5-2019

Design, Fabrication and Test of a Graphene-Based THz Modulator

Ky-el Sanchez
ks3001@rit.edu

Design, Fabrication and Test of a Graphene-Based THz Modulator

By

Ky-el Sanchez

Thesis Submitted
in
Partial Fulfillment
of the
Requirement for the Degree of
MASTER OF SCIENCE IN MICROELECTRONIC ENGINEERING
Approved by

Dr. Ivan Puchades *Advisor*
Assistant Professor, Electrical and Microelectronic Engineering

---

Dr. Parsian Mohseni,
Assistant Professor, Microsystems Engineering

Dr. Santosh Kurinec
Professor, Electrical and Microelectronic Engineering

Dr. Robert Pearson
Associate Professor, Electrical and Microelectronic Engineering
Program Director, Microelectronic Engineering

Dr. Sohail A. Dianat
Department Head of Electrical and Microelectronic Engineering

DEPARTMENT OF ELECTRICAL AND MICROELECTRONIC ENGINEERING
KATE GLEASON COLLEGE OF ENGINEERING
ROCHESTER INSTITUTE OF TECHNOLOGY
ROCHESTER, NEW YORK
MAY 2019

Abstract

One of the most promising approaches to achieve high-speed wireless communication in the terahertz regime is by designing and fabricating devices based on the unique electrical properties of graphene. Certain bands in the THz range (300 GHz – 3 THz) encounter minimal water absorption over short distances and high-speed information transfer is possible. Nonetheless, conventional bulk devices cannot operate at that speed. In the more basic wireless communications system, there are three basic components: a source, a modulator and an antenna. With the use of the Rochester Institute of Technology Semiconductor manufacturing and Fabrication laboratory a graphene-based modulator was designed and fabricated. Electrical testing was performed using the TeraNova THz testbed at the Ultra-Broadband Nano Communication and Networking Lab at the State University of New York at Buffalo.

As proof of concept, a passive modulator was preliminary fabricated following a simple capacitor design. The top plate is an aluminum diffraction grating and couples a THz signal to the underlying graphene monolayer, which acts as the bottom plate. This passive graphene-based device showed a 50% higher absorbance of a 1 THz signal when compared to a device without graphene.

The active modulator was then fabricated and tested. Varying the applied DC bias between the aluminum grating and the buried p+ silicon well, modifies the electric field on the graphene layer and its conductivity. It was found to modulate a THz signal by up to 18 dBm when a +24 Volt bias was applied. These are very promising results for future wireless THz communications and provides practical devices for the THz gap.

Contents

List of Figures

List of Tables

1 Introduction

The internet of things (IoT) is becoming more and more prevalent with the aggressive advancement of technology. This is due to the expansion of technology and communication systems, the internet of things is not only connecting us with other people, but also with our money, our cars and our homes. However, a form of networking and communication is emerging and that is the communication between electrical devices. This is apparent in just the pure variety of devices our phones can connect to at one time [1].

As phones, computers, and other common electrical devices become more prevalent in our everyday lives, new ways in which their respective microprocessors can communicate will need to be realized. More importantly, as more devices move towards wireless communications, there is a need for faster electromagnetic wave communications between those devices. A paper was published in 2010 that spoke of "The Internet of Nano-Things" by *Jornet et al* [1]. This group outlined and reviewed the efforts on how novel nano devices will be integrated in our everyday lives and how they will transmit and receive information from each other [1]. This topic, in general, of nano-networks, contains many potential areas of research from nano networking protocols, information processing and the fundamental nano-scale devices that will operate this network [1].

In the realm of nano scale devices, and using electromagnetic waves to enable wireless communication, it has been found that the most promising area to enable high speed wireless communication over short distances is in the terahertz range [1]. The THz regime ranges from about 300 GHz to 3-4 THz. High information transfer speeds can be achieved because THz signals have a very high bandwidth of 100s MHz. With these large bandwidths, information

transfer speeds have been observed to be about 1 terabit/second.

Over short distances ranging from 1-6 m, the THz regime has a few select frequency ranges that do not encounter high absorption by water [1]. Figure 1.1 shows these select peaks and their transmittance through air at 50% humidity over varying path lengths.

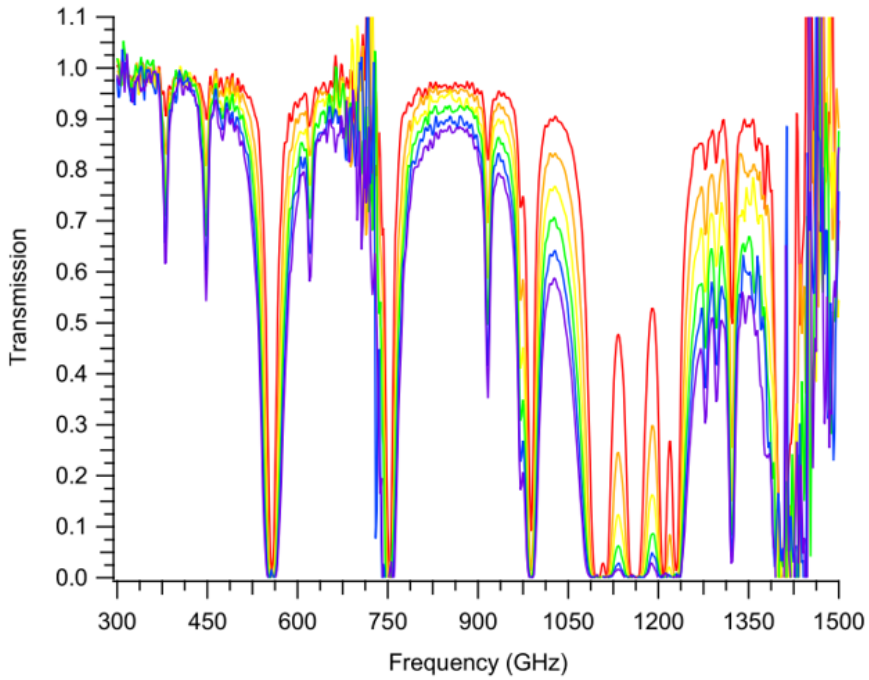

Figure 1.1: THz % Transmission spectra through air at 50% humidity ranging from 0.3 THz (or 300 GHz) to 1.5 THz (or 1500 GHz). The path lengths are from 1-6 m for red, orange, yellow, green, blue, and purple respectively [2].

As seen in Figure 1.1 there is only a high range of THz absorption by water from 1.05-1.25 THz (1050-1250 GHz) and the remainder of the regime experiences high transmission except only in a few select absorption peaks. Peaks at 300 GHz, 750 GHz and 1500 GHz appear to above 100% transmission, this is from low power in measurements causing significant noise in results [2]. From the data, over distances of about 2 m, THz signals can be sent with minimum path loss enabling a reliable short range communication network with very high

bandwidth. Thus, at short ranges, what will limit the information transfer within the THz regime will be the capabilities of the nano devices [1].

Graphene and carbon nanotubes (CNTs) have been the most attractive materials for building nano-devices that can propagate, encode and transmit terahertz signals. It has been found that CNTs can efficiently radiate at the terahertz range [3]. It has also been experimentally confirmed that graphene channel plasmons can couple with terahertz radiation and propagate at a terahertz frequency [1, 4, 5]. Not only can graphene couple with terahertz radiation, it can also modulate it because of the high control that a small applied voltage has over its Fermi level [6].

There has been copious research done in the theory and processing of graphene based devices [3, 7, 8, 9, 10, 11]. This novel 2D material has been so researched because of its high mobility, semi metal behaviors, compatibility with CMOS processing and a multitude of other applications [4, 7, 6]. Within this wealth of research, a relatively newer application has been developed in tuning surface plasmons of graphene and applying it for high speed device communications [12].

These new developments prove to be a very promising field which could allow the transfer of information between devices to be in the terahertz range. The propagation of surface plasmonic polariton waves (SPP waves) under a diffraction grating allows for the coupling of electromagnetic waves at the terahertz frequency and further modulation by an applied voltage [13]. *Jornet et al* [12] published a paper in 2017 describing their research and efforts in simulating such a device. Through COMSOL ® EM wave and RF analysis, it was shown that SPP waves can propagate at the boundary of the dielectric and the substrate [12]. This boundary was electrostatically described by the complex conductivity of a graphene

monolayer. The incoming terahertz wave could then couple with the SPP waves that have been reported to form in graphene [12].

With the findings in the tunable absorption of THz radiation and THz plasmonics in graphene based devices, a wealth of novel devices have been proposed to begin to fill in the THz gap. The general mechanism behind modulating the absorption of THz radiation can be well explained by the increase or decrease in optical intraband transition in the graphene monolayer [14]. However, there is another analytical way to describe the complete absorption of THz radiation through circuit analysis and impedance matching [15]. This is characterized through the use of perfectly matching the free space impedance of the signal and the input impedance of the device [15]. The simplest model that achieves this impedance matching is the Salisbury screen [15]. This general model makes use of a resistive sheet and a quarter wavelength dielectric to completely block transmission. With a graphene monolayer as the resistive sheet, complete THz absorption can be achieved and novel devices can be designed to further modulate this absorption [15].

The first section of this work will be of the theoretical analysis done on the electrostatics of graphene. This will be followed by a discussion of the surface plasmons and optical effects of a graphene monolayer. Then the efforts towards simulating and applying the electrostatics of graphene will be reviewed. Then the final section of this chapter will pertain to the process development of fabricating graphene based devices and how they are made compatible with current semiconductor technology.

Following this review, the work done for this thesis will be discussed in detail. This discussion begins with the design of the THz modulator. Then the fabrication details of both the passive and active THz modulators will be discussed. Following the fabrication of

the devices, test results will be presented. This work demonstrates the successful fabrication and testing of both the passive and active THz modulators.

2 Electrostatics of Graphene

2.1 Graphene's Band Structure

A graphene primitive structure is comprised of six carbon atoms bonded in such a way to form a hexagonal lattice. There are four valence electrons in a carbon atom. Three of those electrons do not contribute to the conductivity of the film because they form coplanar pi bonds to neighboring carbon atoms [9]. The 4th electron is considered to be in the $2p_z$ state and graphene is treated as only having one conducting electron per atom [9].

With the graphene structure, the reciprocal lattice vectors and, subsequently, the Brillouin zone can be defined. Then, linear combination of atomic orbitals (LCAO) can be used to find the respective periodic energy states at certain points within the Brillouin zone [9]. LCAO is a quantum mechanical technique that assumes that the wave function of a given molecular structure is the summation of the respective atoms orbital wave functions. This technique is often used in quantum chemistry to predict the structure of molecules [16]. From the use of the LCAO model, the Coulomb integral, resonance integral and the overlap integral can all be found. These can then be applied to specific points on of the defined Brillouin zone. Figure 2.1 shows the entire graphene band structure.

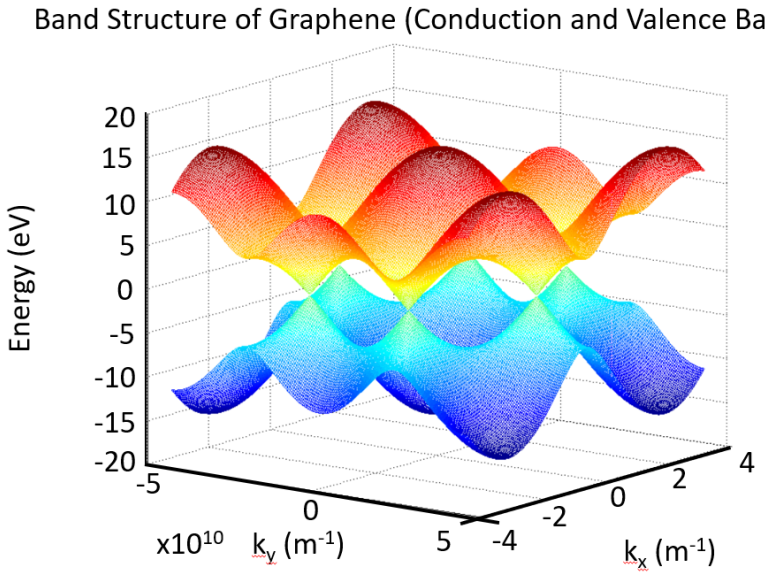

Figure 2.1: Complete view of the Energy bands derived from the LCAO and variations principle method of quantum mechanics of graphene as defined in its Brillouin zone. Each band forms a cone forming the Dirac point[17].

Each level in Figure 2.1 corresponds to higher energy states that the conducting electrons can occupy which creates the potential well around a single carbon atom. These increase outwardly towards the edge of the structure. Each energy level is a summation of the ground energy state of the $2p_z$ electron, and the corresponding expectation value of the orbital exchange energy of the initial atom and the closest neighboring atom [9]. These values were calculated for the Hamiltonian energies. They were also calculated for the isolated atom and lattice potentials.

In un-modulated graphene, the highest and lowest energies of the valence and conduction band meet to form its conical shape with little to no energy gap and a very low density of states in that region, the point where they meet is called the Dirac point [9]. The cross sectional view of graphene's band structure is as shown in Figure 2.2.

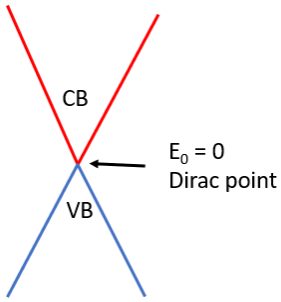

Figure 2.2: Cross section of the graphene band structure where CB is the conduction band and VB is the valence band. The energy gap is zero forming what is known as the Dirac point [6].

Since there is no band gap but also no band overlap, graphene is considered to be a semi-metal [12, 18]. As a semi-metal, it has a high electron mobility but can be easily modulated by applied gate voltages as will be discussed further along in this thesis [6, 19].

2.2 Graphene's Conductivity

With the aforementioned band structure of graphene, the conductivity can be both approximated and also analytically derived as a function of the applied electric field's frequency ω and the electron wave vector k [9, 20]. Qualitatively, and as an approximation, the outer most energy states along the hexagonal ring of the Brillouin zone can be found by integrating over the energy gradient over an interval dE. Then, the density of states is calculated with the Fermi-Dirac distribution and calculating the effective number of electrons per atom. Subsequently, the electron flux, which is often referred to as the current [9], can be attained by solving the Fermi Dirac distribution in the presence of an electric field [9]. The current can be defined as the integral of Fermi Dirac distribution multiplied by the applied voltage, integrated over the scattering probability which would be a function of lattice sites and therefore the energy contours as defined by the band

structure [9]. After this the approximate constant value of the in-plane conductivity $\sigma_{||}$ was found by averaging over all directions of the applied field in the plane of the layer [9] and expressed as Equation 2.1 [9].

$$\sigma_{||} = \frac{16\pi e^2 \tau}{h^2 c} kTlog(2) \tag{2.1}$$

Where h is Planks' constant, c is the atomic distance, k is Boltzman's constant e is the charge of an electron and τ is the relaxation time. This conductivity is an average over all directions and is a constant value.

The analytical conductivity of graphene can be defined as a summation of the inter and intra band contributions [20]. However, the actual derivation is out of the scope of this work. Qualitatively, the conductivity is derived by a similar technique as equation 2.1 by solving for the current. However, in this analytical approach, averaging techniques were not used and the external field applied is treated as an actual vector potential as opposed to a constant value [9, 20]. Because of this, the particle flux and therefore the conductivity must be solved using a statistical mechanics technique in which the states are solved periodically and with the presence of a constant application of energy [21]. This is called the Gibb's ensemble and must be averaged over to attain the respective energy states in the presence of the vector potential [21]. This is done through by putting the equations in the form of the temperature Green's function [20]. The temperature Greens' functions solves a quantum field systems at finite temperatures, the details of which will not be covered in this thesis [22]. Through this work, it can be shown that at room temperature and at high carrier concentrations graphene acts as a semi metal and its conductivity is dominated by the intra band contribution. It is

considered a Drude like conductivity and is well described by the equation 2.2 [12, 20].

$$\sigma^{g}_{intra}(\omega, k) = \frac{i2e^2}{\pi\hbar^2}\frac{k_B T}{\omega - i\tau_g^{-1}} ln(2cosh(\frac{E_F}{2k_B T})) \tag{2.2}$$

Where e is the electron charge, $\hbar$ is the reduced planks constant, k_B is Boltzman's constant, T is the temperature, E_F is the Fermi energy of the graphene sheet, τ_g is the relaxation time of the electrons and ω is the frequency of the applied electric field driving the current. As a partly imaginary number, graphene has an AC conductivity. The intra band term, shown in equation 2.2, is the dominating term at room temperature and lower impurity doping. This equation is of the same form of the Drude conductivity used to describe semi-metals. This equation can be reduced to its imaginary and real parts and plotted with changing frequency within the THz regime and with varying graphene Fermi energy. Figure (2.3) shows a plot of the real and imaginary parts of graphene's Drude like conductivity

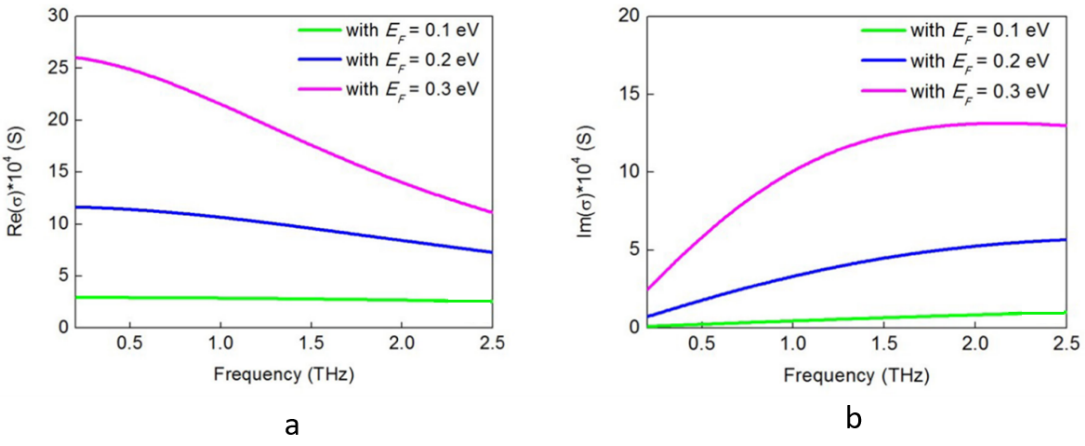

Figure 2.3: Graphene's real (a) and imaginary (b) parts of its intraband Drude like conductivity and its dependence on its Fermi energy and its frequency [23].

From Figure 2.3 the conductivity's dependence on the graphene's Fermi energy and its frequency is apparent [23]. With increasing Fermi level, there is an increase in its conductivity which is analogous to an increase in carrier concentration [23].

2.3 Electrostatic Tuning of Graphene

The electrostatic tuning of graphene occurs through the phenomenon of charge doping of the graphene monolayer. The mechanism is well modeled through electrostatics as well as density functional theorem (DFT) calculations [6]. DFT is a series of quantum mechanical approximation techniques used for solving quantum mechanical many-body problems [6]. Charge doping is characterized by the shift in Fermi level by an applied voltage. *Bokdam et al.* derived a model for this and began by defining a generic semiconductor capacitor stack as seen in Figure 2.4 [6].

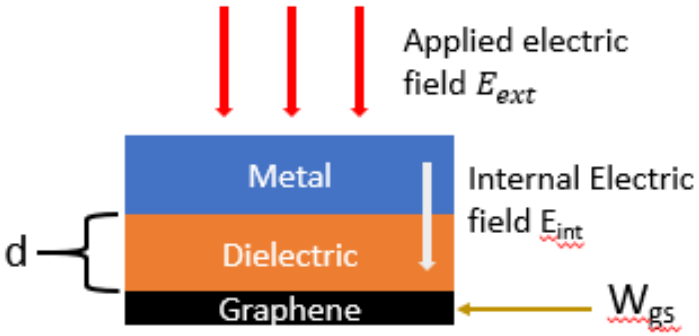

Figure 2.4: Device structure used to model the change in Fermi level of a graphene monolayer in the presence of an electric field [6].

With a given work function of the graphene and the stack, *Bokdam et al.* simply stated

the shift in the Fermi level with respect to the charge neutrality point as

$$\Delta E_F = W - W_{Gr} \tag{2.3}$$

Where W is the work function of the stack and W_{Gr} is the work function of the graphene [6]. The work function of the stack can be expended as the difference between the work function of the metal and the change in voltage across the stack at charge neutrality [6]. This change in voltage was then defined as

$$\Delta V = -eE_{int}d + \Delta_{M|D} + \Delta_{D|Gr} \tag{2.4}$$

e is the charge of the electron, E_{int} is the internal electric field, d is the dielectric thickness, $\Delta_{M|D}$ and $\Delta_{D|Gr}$ are the potential steps across the stack [6]. These potential steps come from the bonding between each material interface where dipoles form [6]. However, the magnitude of these dipoles is minimal compared to that of the rest of the system. Thus, *Bokdam et al.* treated these potential steps as independent of the applied electric fields and confirmed this assumption with DFT calculations [6]. Following this, the surface charge density ρ of the graphene sheet can be defined electrostatically as a combination of the applied external and internal electric field [6]

$$\rho = \epsilon_0(E_{ext} - \kappa E_{int}) \tag{2.5}$$

κ is the relative dielectric constant of the dielectric layer, ϵ_0 is the permittivity of free space and E_{ext} is the externally applied electric field. The external electric field was treated as an independent variable to be able to properly model the shift in Fermi level as a function of

the applied field [6].

The surface charge density can also be defined by the shift in Fermi level. Charge is injected into the graphene monolayer by first filling up states close to the charge neutrality point, which is the Dirac point of the graphene band structure [6]. The band structure of a semi metal monolayer of graphene is conical at this charge neutrality point, and meet such that there is no band gap. This leads to a very low density of states [18]. Therefore, the surface charge density at these conical points, where the charge doping occurs, is described by [6]

$$\rho = e \int_0^{\Delta E_f} D(E) dE \tag{2.6}$$

Since the density of states $D(E)$ at these points is very low [9], $D(E)$ can linearly approximated as

$$D(E) = |E| D_0 / A \tag{2.7}$$

Where E is the energy, A is the area of a graphene unit cell, D_0 is the initial density of states, which is a constant value dependant on the Brillioun zone grid used when performing these electrostatic calculations. The value used by the authors was 0.102 (states/eV^2 unit cell) and the Brillouin zone grid was 36×36 N, where N is number of Brillouin zones used in the DFT calculations [6].

Solving for the surface charge density with the approximation of the density of states, then combining equations 2.3-2.5, the change in the Fermi energy, with respect to an applied electric field E_{ext} can be modeled as [6, 12]

$$\Delta E_f = \pm \frac{\sqrt{1 + D_0(e^2/(\epsilon_0 A))(d/\kappa)^2 |e(E_{ext} + E_0)|} - 1}{D_0(e^2/(\epsilon_0 A))(d/\kappa)} \tag{2.8}$$

Where ϵ_0 is the permitivity of free space, κ is the dielectric constant of the dielectric layer, d is the thickness of the dielectric layer and e is the charge of an electron. The sign of the change in Fermi energy is dependant on the sign of the term $E_{ext} + E_0$. E_0 is the internal electric field across the dielectric when there is no applied electric field [6]. Equation 2.8 was confirmed by DFT techniques and accurately models how the Fermi level of a graphene monolayer can be tuned electrostatically with a metal gate through charge doping.

The control that the metal gate has over the fermi level shift in equation 2.7 is embodied by the E_0 term. This is the electric field across the stack and is determined by the potential steps across the layer. The expanded form of the values is

$$E_0 = \frac{\kappa}{(d)(e)}(W_m - W_{Gr} - \Delta_{M|D} - \Delta_{D|Gr}) \tag{2.9}$$

Which was extracted from equations 2.3 and 2.2. The significance of this is found in the potential drops across the metal to dielectric and dielectric to graphene monolayer. This model only pertains to metals where the graphene absorption to their surface is dominated by van Der Waals interactions [24]. This generally weaker bonding, does not destroy the characteristic conical points of the graphene band structure. It has been calculated that, with direct contact between graphene and metal, Al, Cu, Ag, Au, and Pt bind to graphene in such a way and preserve its conical form. However, most of these metals cause an immediate positive or negative shift in the fermi level of graphene. The metal that causes the least amount of shift in the fermi level has been found to be gold [24].

This retention of the fermi level allows for an increase in modulation range because it does not fill up empty states at the conical points with initial interaction [24]. This maximizes

the range that an applied electric field has over the shift in fermi level.

3 Surface Plasmonics in Semiconductors

Plasmons are often described as 2D electrons that still follow Dirac statistics [5, 12, 13]. The mechanism of plasmonic wave generation in the channel regions of nano devices that exhibit semi metal characteristics such as high mobility and low electron to nucleus collisions, was found to be well described by shallow water hydrodynamic equations [4]. Qualitatively, this is because the electron reflection at the boundaries of the channel creates a standing wave which is not damped by depth just as in the hydrodynamic case. Due to the high concentration of electrons, the electron surface concentration of such a channel is

$$n_s = CU/e \tag{3.1}$$

Where C is the gate capacitance per unit area, e is the charge of the electron and U is the gate to channel voltage [4].

The Euler's equation of motion

$$\frac{\delta v}{\delta t} + v\frac{\delta v}{\delta x} = -\frac{e}{m}\frac{\delta U}{\delta x} \tag{3.2}$$

constrained by the continuity equation

$$\frac{\delta U}{\delta t} + \frac{\delta U v}{\delta x} = 0 \tag{3.3}$$

where $v(x,t)$ is the local drift velocity and m is the mass of an electron, can be applied to describe the motion of the electrons in the channel regions. These equations match that of

the hydrodynamic equations of shallow water [4]. Where the electron velocity corresponds to the fluid velocity, eU/m corresponds to the term gh where g is the force of gravity and h is the depth. This mechanisms is often cited in literature as the Dyakonov and Shur shallow water analogy [4, 5, 25, 26]. The linear solutions of these equations yield the wave equations of the surface plasmons and their respective frequencies. From this analogy Dyakonov and Shur were able to theorize terahertz radiation and coupling in high electron mobility materials [4].

3.1 Terahertz Coupling to Graphene Plasmons

The shallow water analogy developed by Dyakonov and Shur has been applied to graphene's plasmonic behavior to prove the propagation of surface plasmons at the terahertz frequency [4, 12, 25]. Fundamentally, this model works because of graphene's Drude like conductivity in a state of high carrier concentration. This has been further developed by *Peres et al.* who analytically modeled how an incoming incident electromagnetic wave couples to the graphene plasmons with the presence of a diffraction grating [13].

Their model solves the wave equations with the graphene on top of a grating, this was done to achieve a more complete set of equations for the system as shown in Figure 3.1. With the graphene on top, the directionality of stress has a larger contribution to the position dependent conductivity. They state that a similar result can be found with a top grating [13]. However, there will be energetic relaxation as the EM wave passes through the grating to the graphene monolayer. Also, there will be a much smaller conductivity contribution from stresses at the corners of the grating where the film will sag [13]. The model begins with a grating with given period d, line width r, line height h, incident angle θ and the

grating material dielectric constant ϵ on top of a graphene monolayer as shown in Figure 3.1 [13]. The graphene monolayer is considered to be charge doped, therefore have a high electron concentration, as well as be under low stress and lay flat. The analysis deals with solving the resulting wave equations in the trench and grating regions to quantify the total absorption, transmission and reflection of the incident electromagnetic wave by the graphene plasmons.

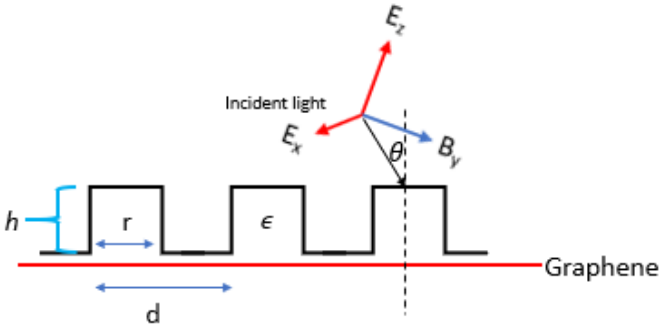

Figure 3.1: Model of square wave grating with a graphene monolayer underneath with an incident electromagnetic wave with a frequency of 1 THz [13].

With the electromagnetic waves having the following components $\mathbf{B} = (0, B_y, 0)$ and $\mathbf{E} = (E_x, 0, E_z)$ the exact equations can be solved for the grating areas. This is made easier by noting that the boundary conditions of the problem follows that of the Kronig-Penny band theory model of solids [13]. Thus, this model has exact solutions if the electrodynamic equations describing the system can be put in a form that matches the Schrödinger equation for the Kronig-Penny model [13].

The analysis begins by solving first for the wave equation within the grooves themselves. Then, solving for the transfer equations across the boundaries with consideration of the change in dielectric constant due to the position dependent conductivity of graphene [13]. Following that work, solution to the scattering of the incident wave is solved and that yields a

series of solutions dependant on the number of eigenvalues chosen. For most of the plotting of their models, this number was chosen to be 20 because it was the minimal number needed to accurately describe the magnetic component of the EM wave [13]. These solutions can be re written as transmittance and reflectance equations which can then be written as absorbance. They plotted these equations with respect to frequency of the incoming radiation. Figure 3.2 shows their results

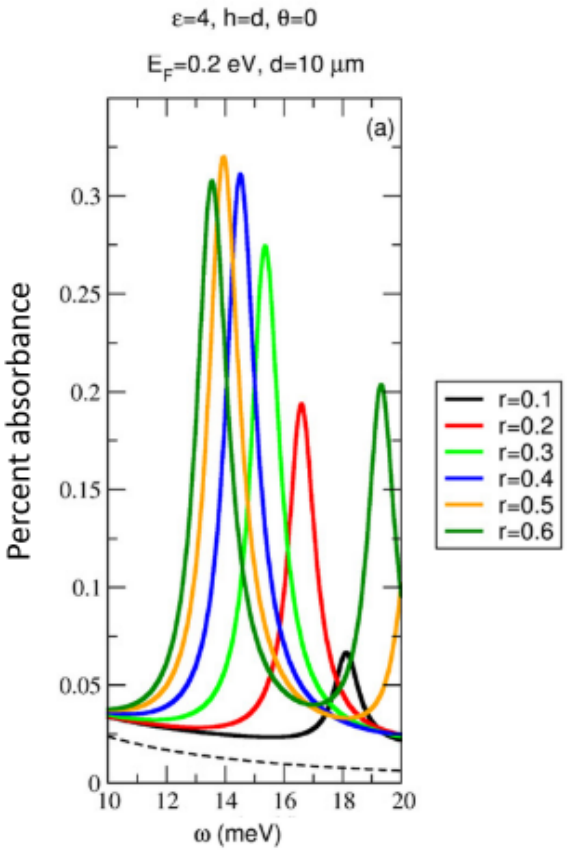

Figure 3.2: Calculated absorbance results at energies corresponding to 2 THz (10meV) to 5 THz (20 meV) with varying grating width and in which the grating height was scaled to equal to the grating pitch. Thinned dashed line is at r=1 [13].

.

At 14 meV or 3.3 THz, and $r = 0.5$ μm there was a max absorption peak of 30% when

$h = d$ where $d = 10$ μm. This value was then maximized at $h = 2d$ and the absorption at this value was 45% [13].

3.2 THz Propagation in Graphene based Structures

With the study of THz electromagnetic wave propagation in a graphene monolayer, a conglomerate of work has been done to confirm the theory and record successful propagation of graphene plasmons at THz frequencies. A series of papers have been released that described the efforts of graphene plasmonics in the terahertz range [5, 18, 26, 27, 28, 29]. The research published has been successful in propagating a terahertz signal in a graphene monolayer, characterizing the charge dynamics in graphene, and achieving experimental data on terahertz plasmonics.

Most of the work use similar structure in which graphene sits atop silicon dioxide and is exposed with near infrared light [5, 18, 27]. From this near field imaging was used to measure the localized electric field of the oscillating SPP waves in the graphene monolayer and its respective tunability with an applied voltage [5, 18, 27]. The difficulty of measuring graphene plasmons resides in matching the wave-vectors of the IR photons with that of the graphene plasmons without optical techniques such as diffraction gratings [5]. Using IR near field imaging, Dirac plasmons behaviors caused by scatterings by the vibrations in an SiO_2 layer, can be measured and quantified [27]. *Fie et al.* published results describing the increase of the IR near field amplitude in arbitrary units $s(\omega)$. Figure 3.3 shows some of their results [27].

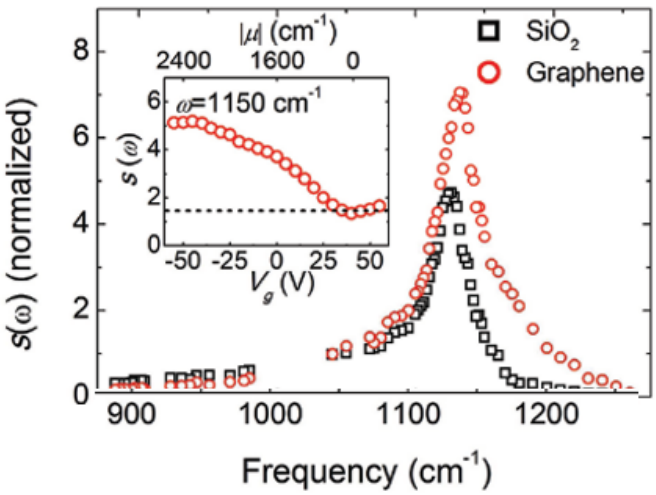

Figure 3.3: Results attained by *Fie et al* in which the near field amplitude was measured with graphene atop of silicon dioxide (red) and with only silicon dioxide (black). At the peak frequency, the near field amplitude was also measured with a changing applied voltage Vg (minigraph) [27].

From these results it is clear that, not only is there high near field amplitude of SPP waves at the the relevant IR frequency, but at this frequency modulation is attainable. The difference between SiO_2 and graphene is clear and, along with the modulations, shows the dependence of these oscillations to carrier concentration.

The modulation of the graphene plasmons were also further investigated in a later Nature paper by the same group *Fei et al.* [5]. In their work they research the effect the gate voltage had on the near field amplitude and corresponded that to the wavelength of the SPP wave. Table 1 summarizes their results:

Gate Voltage	**-10V**	**0V**	**10V**	**20V**	**30V**
SPP wavelength λ_p	260nm	240nm	230nm	215nm	180nm

Table 1: SPP wavelengths attained through near field amplitude measuring and their changes with applied voltages [5].

Graphene plasmons response to IR radiation has been used to illustrate the charge dynamics of a graphene monolayer and confirm much of the electrostatic theory developed in section 2.2. The group *Li et al.* placed graphene atop of 300 nm of SiO_2 and was contacted by Cr/Au and then exposed with an infrared light with a synchotron source [29].

They first measured the transmitted and reflected infrared light at varying modulation voltages normalized by the reflectance and transmittance from the underlying oxide layer [6]. Because of graphene's high response to infrared light, they were able to obtain optical constants from the graphene monolayer by running photo-emission experiments on their sample [29]. With the optical constants, which varied depending on the applied voltage, they were able to make measurements of the optical conductivity and then calculate out the respective Fermi level [29]. This Fermi level was all in relation to the threshold value of $2E_f$ at differing wavelengths of the infrared light [29]. The Fermi level of $2E_f$ is considered to be the onset of the interband contribution and its dominance over graphene's Drude like conductivity [29]. Figure 3.4 shows some of the results of their work and confirmation of the graphene band structure.

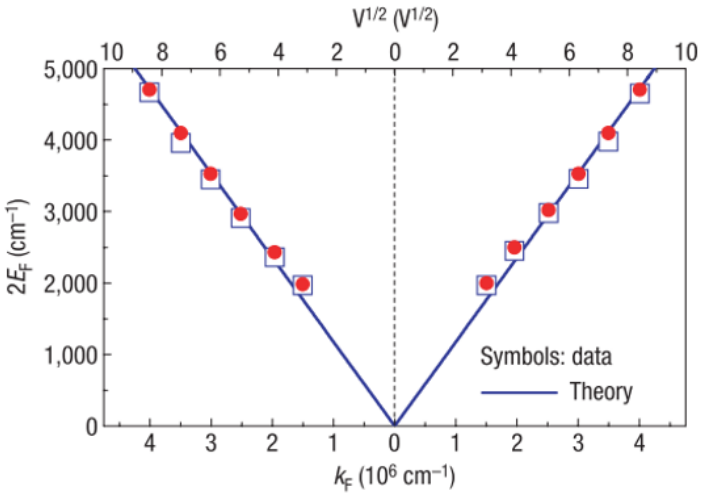

Figure 3.4: E K diagram of the graphene band structure and the experimentally measured points of the 2Ef and K points found through an increasing or decreasing applied voltage of $\sqrt{V}$ [29].

Figure 3.4 affirms the theoretical work done so far on graphene plasmons and graphene electrostatics. The work that produced Figure 3.4 utilized all the physical characteristics and theory mentioned by this thesis. The proportionality found of the Fermi level on $\sqrt{V}$ confirms the charge doping mechanism described in section 2.2.3. Their experimental data shows the conical nature of the band structure. Also, the techniques they used to quantify their results all made use of the surface plasmons of graphene and its relationship on THz radiation.

4 Simulated and Fabricated Terahertz Modulator Devices

4.1 Simulated Graphene based Terahertz Modulator

In communication networks, there are three basic components. A source, a modulator and an antenna. Other work has researched and reviewed the efforts of THz sources and antennas [1, 3, 30, 31]. A range of THz sources have been made [30]. *Lewis et al.* cites that the more promising ones are based on surface phenomena such as optical rectification, transient surface currents and THz surface emission through mechanical movement [30].

THz detectors and antennas have also been a focus of research [1, 3, 31]. some of the more promising antennas are CNTs because of their ability to radiate and absorb signals in the THz range [1, 3]. Thus they have proven to be a viable low power option for THz detection and emission [1].

This work focuses on the modulator component for THz signals. In a communications network, the modulator receives electromagnetic waves, or signal, and applies an electric field to change the amplitude of frequency of that signal. The basis of this work is an amplitude modulator that modulates with an applied voltage.

Simulations of a THz modulator have been done in previous work [12, 32]. In the work done by [32], an AlGaAs/InGaAs/GaAs heterostructure with planar gold lines on top was simulated on CST micro wave studio®. THz radiation passed through the 2DEG and a modulating signal was applied to the gold lines. The 2DEG behavior was captured by the use of the classical Drude model conductivity similar to equation 2.2, which was applied at

the boundaries of the heterostructure and the gold lines [32]. Figure 4.1 shows the simulated structure.

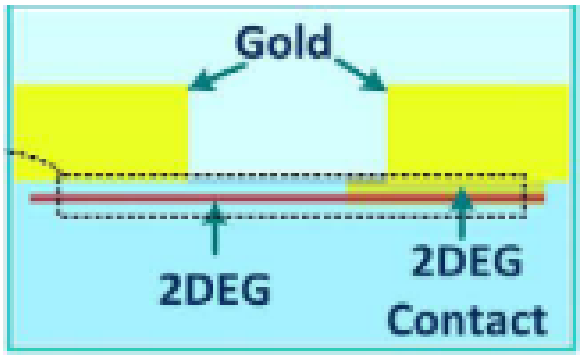

Figure 4.1: CST microwave studio simulated THz modulator with the use of a 2DEG and gold contacts for the modulating signal [32].

This simulation predicted a modulation depth of 18 dB at 0.2 THz and 13 dB at 1 THz [32]. It was also found that an increase in the channel length led to an increase in THz modulation [32].

With the given theoretical development of a graphene based THz modulator, a series of simulations were also run to further realize the devices' operation. Dr. Jornet spear-headed these simulations on COMSOL multi-physics to show that, when illuminated with a terahertz signal, the structure shown in Figure 4.2 will propagate surface plasmonic polariton waves with differing structural parameters. These parameters include dielectric thickness, grating pitch, grating thickness and the incorporation of different materials for both the metal grating and the dielectric layer.

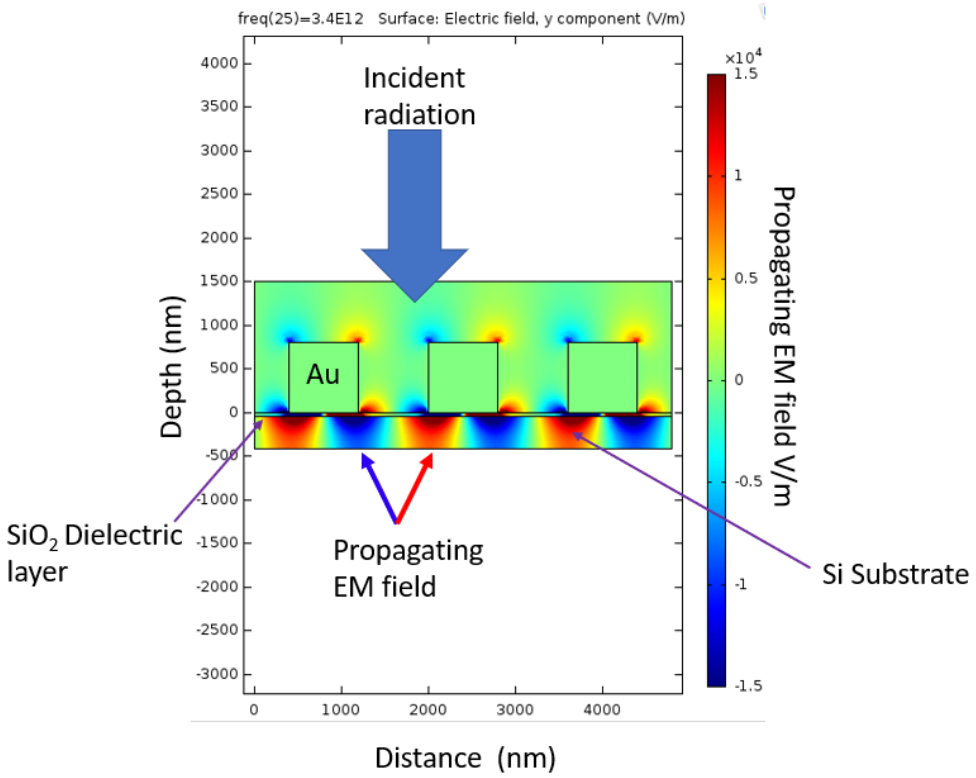

Figure 4.2: COMSOL simulated device structure illuminated with an electromagnetic wave with frequency 3.4 THz with a pitch of 1600 nm and a grating thickness of 800 nm and the resulting electromagnetic field from the propagating SPP waves [12].

The way the simulation works is by the electromagnetic wave module in COMSOL multiphysics [12]. The device model is of a metal grating which sits on top of a dielectric which is on top of a substrate. Since COMSOL does not incorporate atomic simulation nor solves the Schrödinger equation in the defined regions of the mesh, a graphene monolayer cannot be directly simulated in the device structure. Instead, the boundary layer between the dielectric and the substrate is defined by the Drude model complex conductivity of a graphene monolayer (equation 2.1) [12]. With this equation for conductivity, COMSOL can then reliably simulate the movement of surface plasmons, their coupling with the EM wave and the resulting SPP wave. It does this by recalculating the change in conductivity with

the presence of the EM wave. The changes in aspects such as dielectric thickness, material and grating period are all incorporated in the τ term defined in graphene's intraband Drude like conductivity, which is the relaxation time of the carriers as shown below [12].

$$\sigma^{g}_{intra}(\omega, k) = \frac{i2e^2}{\pi\hbar^2}\frac{k_B T}{\omega - i\tau_g^{-1}} ln(2cosh(\frac{E_F}{2k_B T})) \tag{4.1}$$

From the results of these simulations it was found that both the grating pitch and the Fermi energy set for the graphene had significant effects on the the SPP wavelength and amplitude. An increasing grating pitch from 400 nm to 1600 nm led to increase in SPP wavelength but a decrease in SPP wave amplitude as shown in Figure 4.3

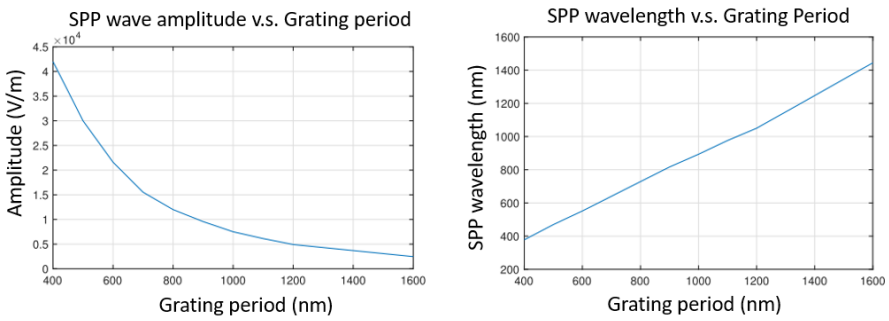

Figure 4.3: Simulated results of the grating pitch effect on both SPP wavelength and SPP wave amplitude [12].

The same was done for the effect Fermi energy has on the propagating SPP wave as shown in Figure 4.4

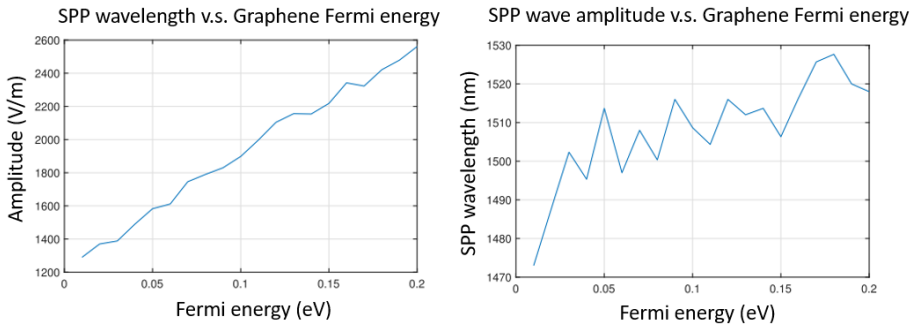

Figure 4.4: Simulated results of the effect the graphene Fermi energy has on both SPP wavelength and SPP wave amplitude [12].

It is clear that both the Fermi level and grating pitch affect the SPP wave which follows with the developed theory. The parameters of grating period and, indirectly, Fermi energy were tested in this thesis and will be described further in the results section.

4.2 Fabricated and Tested THz Modulators

Terahertz modulation has been achieved only a few times [19, 33, 34]. It has been done both electrically and optically by a few research groups in their pursuit of THz modulation and in attempts to access the THz bandwidth for faster information processing speeds. Their efforts have contributed to furthering terahertz technology, however, the devices failed in either practicality [33], acceptable depth of modulation [19] or electrically driving the modulation [34]. Another problem with the devices fabricated in [19, 34] and other research done [35, 36], is that they are based on the transmission of the terahertz radiation as opposed to the absorption and propagation of the signal. This limits the capabilities of further modulation and directing information to other devices [1].

One of the earlier modulators proposed followed a similar design to this work, which utilized the depletion or accumulation of carrier densities in a high mobility semiconductor

to modulate an incoming terahertz signal. The structure was comprised of Schottky grating on top of n-type GaAs layer, which provided a series of quantum wells. The structures of these wells were designed for the absorption of THz radiation through electron excitation which inherently absorbed the terahertz signal. With the application of a negative bias, the signal could be modulated [33]. Figure 4.5 shows the structure of the device.

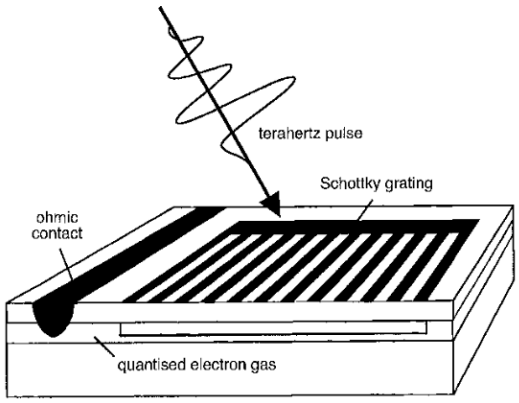

Figure 4.5: Terahertz modulator which utilized quantized states to enable absorption of a terahertz signal and an applied voltage to modulate that signal [33].

However, to maintain the structure of the quantum wells, this device could only operate at a temperature of 10 K [33]. This presents a series of difficulties when pursuing further application in electronic devices.

With a similar device design another THz modulator has been researched and fabricated. This one was based on the depletion of 2DEGs created by the potential wells in AlGaAs and GaAs hetero-structures. Metal contacts were formed on top of the hetero-structures and then illuminated with THz radiation. The transmitted THz wave was measured with and without modulation [19]. However, the modulation depth was found to be 3%, which was considered to be minimal and their future work hoped to discover higher range of modulation [19].

A more successful THz modulator had been fabricated that was based on a graphene monolayer similar to the current research presented here [34]. The device structure was a graphene monolayer atop a germanium substrate and the modulation was driven by a continuous wave laser with low photo-doping power [34]. It achieved a modulation depth of 94% and achieved a band width of THz transmission of frequencies ranging from 0.25 THz to 1 THz [34]. The device design and operation can be seen in Figure 4.6.

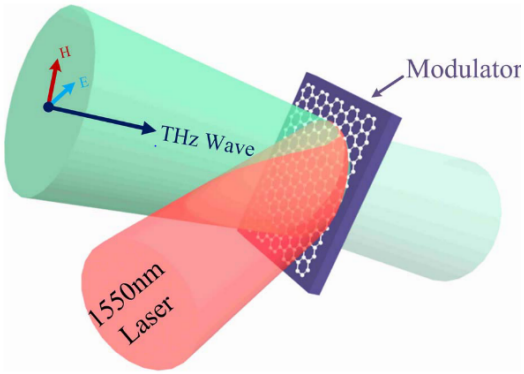

Figure 4.6: Terahertz transmission modulator which uses a graphene monolayer atop a Germanium substrate and modulates with a CW laser with low photo doping power [34].

However, this device is all optical, which means it would be limited, for obvious reasons, in its application for electrical circuits [19]. It also relies on the transmission of the THz signal and does not work to absorb it for further modulation.

Again with a similar design to that of the work discussed, *Sensale-Rodriguez et. al.* released a paper describing their fabricated and tested graphene based THz modulator. The device consisted of a back metal electrode, p-type doped silicon, a silicon dioxide layer, a graphene monolayer and a gold top gate in which a DC bias is applied across the stack. The device was illuminated with a source that varied in frequencies from 570-630 GHz. The reflected power was then measured at points of varying voltages. Figure 4.7 shows the

normalized reflectance at applied DC biases.

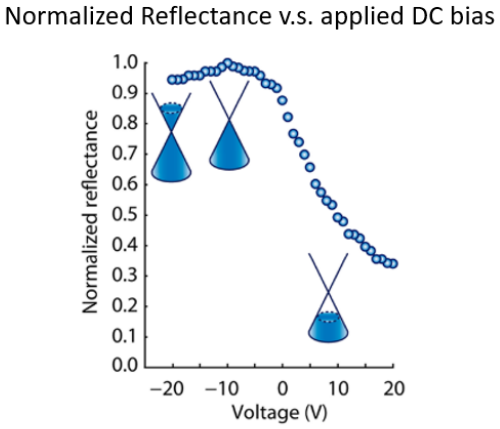

Figure 4.7: Normalized reflectance of a Graphene based THz modulator with a 0.6 THz source incident on the device and an applied bias of -20 V to 20 V [37].

From Figure 4.7 it was reported that successful THz modulation was achieved with the application of a positive voltage. The drawn band structures in Figure 4.7 show the physical operation of the device. Close to 0 V there is a minimum in THz absorption because of the few low energy intraband transitions that can occur [14, 38]. This minimum in intraband transitions is due to the few states available for carriers at the Dirac point in the band structure. However, as the Fermi level gets tuned up and down with hole or electron doping, more intraband transitions can occur allowing for an increase in THz absorption [37]. It is expected that as a more negative bias is applied to the device, Figure 4.7 will begin to look more symmetrical about the Dirac point [14, 15].

Other non-2D material based THz devices have also been fabricated in the pursuit of THz modulation. Some of the work done is reviewed by *Han et. al.* whom hope to fill in the THz gap with silicon based devices [39]. One of their proposed devices is a THz source using a 1 THz radiator array. This device works through the combination of low THz

(0.2-0.4 THz) radiators which have integrated antennas. These THz sources are generally SiGe hetero-junction bipolar transistors (HBT) which can perform as a 250 GHz oscillator. Due to the repeatability of CMOS processing, the sources can be designed to all share same frequencies and phases, which can yield a high intensity 0.2-0.4 THz beam. They can also be designed to extract the fourth harmonic and achieve a 1 THz beam.

With the combination of many radiators and optical techniques, higher frequencies of up to 1 THz can be radiated on chip. The general mechanism to achieving higher frequency radiation is through the use of a non linear phenomena called high harmonic generation. This is described by the excitation and relaxation of carriers by incoming light [39, 40]. More specifically, the carriers are excited away from the atoms' nucleus and decelerate, they then further recombine with the nucleus of the atom to produce a photon. This photon will have an energy equal to the sum of the deceleration and recombination of the excited electron [40]. However, only a fraction of the lights' intensity excites carriers in this way [40].

In the devices made by *Han et. al.*, multiple arrays were used to filter out the harmonics 1-3f_0 and increase the intensity of $4f_0$. This is done by using the harmonic generation of the 250 GHz fundamental oscillation of the SiGe HBT. Then using a slotted array in which the 1-4f_0 harmonics oscillated, it was measured that the 1-3f_0 standing waves experience complete destructive interference in the vertical and horizontal slotted regions [39]. However, the $4f_0$ standing wave experienced constructive interference in the horizontal slotted region and destructive interference in the vertical regions [39]. This retention of the $4f_0$ harmonic can be seen in Figure (4.8).

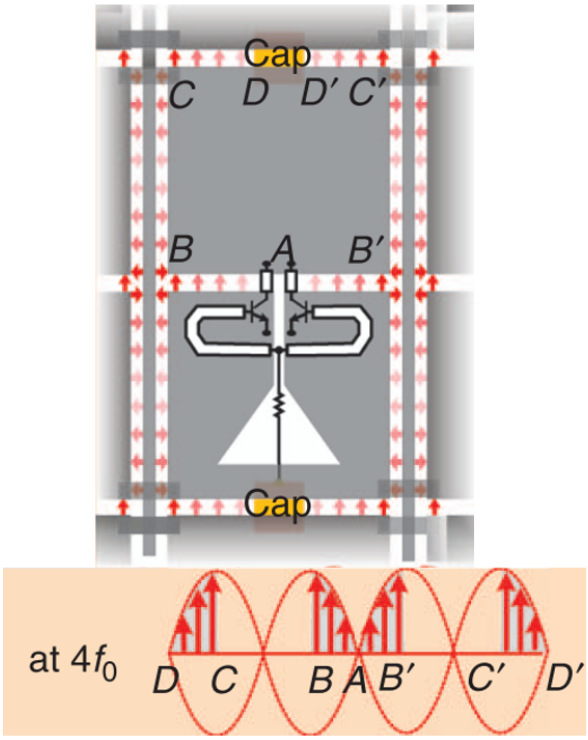

Figure 4.8: Two SiGe HBT operating at a fundamental frequency of f_0=250 GHz driven THz source in which the $4f_0$ harmonic electromagnetic standing wave is retained and amplified through the use of multiple arrays. This harmonic experiences constructive interference in the horizontal regions of the array slots. The arrows shown in the slots are the electric fields in that region

This device structure can be further modified geometrically to induce phase or amplitude modulation of the 1 THz signal [39].

5 Processing of Graphene Monolayers for Device Fabrication

The following section will focus on the process techniques used for the fabrication of graphene based devices. Due to its mechanical fragility, and the fact that it is a single monolayer, special techniques are used to reduce impurities in the monolayer, folds and wrinkles as well as to place it on given substrates. This section will review these processes as many of these techniques were utilized in the fabrication of the graphene based THz modulator.

5.1 Chemical Vapor Deposition (CVD) Growth of Graphene

There are only a few methods of growing a monolayer of graphene that yields a uniform film with minimal defects [41]. One of the most reliable and scalable ways to do this is through the chemical vapor deposition (CVD) growth of the graphene monolayer on a copper foil substrate [42, 43]. The solubility of carbon in copper has been reported to be >0.001% and it has an inability to form a carbide [42].This is what enables the uniform and controlled growth of the graphene monolayer [41].

The mechanism of this growth is described by the decomposition of methane on a copper foil and carbon surface diffusion on copper. An optimized partial pressure of methane is pumped into the chamber and is thermally decomposed [42]. There is an optimum decomposition rate because if the methane decomposes too quickly leading to high concentration of carbon atoms in the nucleation sites, then multi-layer graphene will form [41]. Copper is most commonly used because of its inability to form carbides [42, 43]. This allows for a slower decomposition of the methane and lower concentrations of carbon

atoms at nucleation sites. This inability to form carbides also allows for high surface diffusion and a greater dispersion of the carbon atoms to further enhance monolayer growth [42].

The CVD process is controlled by the diffusion of carbon atoms along the copper substrate surface [43]. The diffusion rate is then determined by the temperature and partial pressure of the hydrocarbon gas and has a direct effect on the number of layers of graphene [42]. Experiments have been done to characterize the minimum flow of methane at a given temperature to completely cover a Cu foil. It was found that a flow rate of 8 sccm of methane at 980 °C and a total pressure of 750 mTorr was this minimum, and these are used in most systems [41, 43, 42].

5.2 Graphene Transfer Process

With the growth of large area graphene monolayers on copper, techniques are required to move the monolayers onto complementary metal oxide semiconductor (CMOS) process compatible substrates. Transferring these graphene monolayers posses a challenge because of the need to minimize cracks and folds in the film as well as to place it on the substrate with minimal wrinkles and topology. Many experiments have been done to achieve the purest and most uniform transfer process from copper [11, 42, 44, 45].

The most common method of transferring a graphene monolayer is through a poly-methylmethacrylate (PMMA) mediated process [42, 44, 45]. This consists of coating the graphene monolayer with PMMA onto the graphene monolayer and copper stack. Then subsequently etching away the transition metal, cleaning the PMMA/graphene stack and

transferring it to an insulating substrate at which point the PMMA is dissolved. This process has been cited as the most popular due to its relative simplicity as well as its ability to yield minimal defects in the graphene film [11, 44].

Liang et al. developed a clean process of transferring the graphene monolayer to a hydrophillic substrate [44]. This process was developed because it was found that the standard method of etching the copper foil and transferring the PMMA and graphene stack led to interstitial defects and ions between the graphene and substrate layer [44]. These defects greatly reduced the electronic properties. The presence of these defects led to a higher concentration of scattering sites, which decreased the electron mobility in the graphene film [44]. This technique also led to mobile and trapped charges, which have direct effects on threshold voltages and gate control [44]. Therefore, a new process had to be developed to further optimize the transferring of the graphene film [42].

The process proposed by *Liang et al.* follows similar steps of a RCA clean. The process begins with coating PMMA 495 A4 at 3000 rpm to ensure a uniform film and coverage over the entirety of the Cu foil. The PMMA is not hard baked in order to reduce polymer residue when the PMMA is removed [44]. During the CVD growth process of the graphene monolayer, graphene grows in all locations of the copper foil including the back. Therefore, for a controlled and efficient copper etch, the graphene is removed from the backside of the foil with an oxygen plasma etch, after the PMMA is spun on [44]. In the described process, the Cu was etched in a solution of iron nitrate. This etch step is reported to leave residual metal particles in the graphene and PMMA stack [44]. To minimize the presence of these metal particles, a solution of de-ionized (DI) water, hydrochloric acid, and hydrogen peroxide is mixed 20:1:1 respectively. This step is reported to thoroughly remove residual metal that

may have been left on the PMMA and graphene stack [44]. Subsequently, the graphene and PMMA stack is rinsed in a DI water bath and then placed in a DI water, ammonium hydroxide and hydrogen peroxide 20:1:1 to remove any organic particulates. Then, it is followed by a rinse in which the stack is transferred to the desired substrate and the PMMA is dissolved in acetone for 15 minutes then choloroform for 24 hours [44]. Figure 5.1 shows the steps of the process:

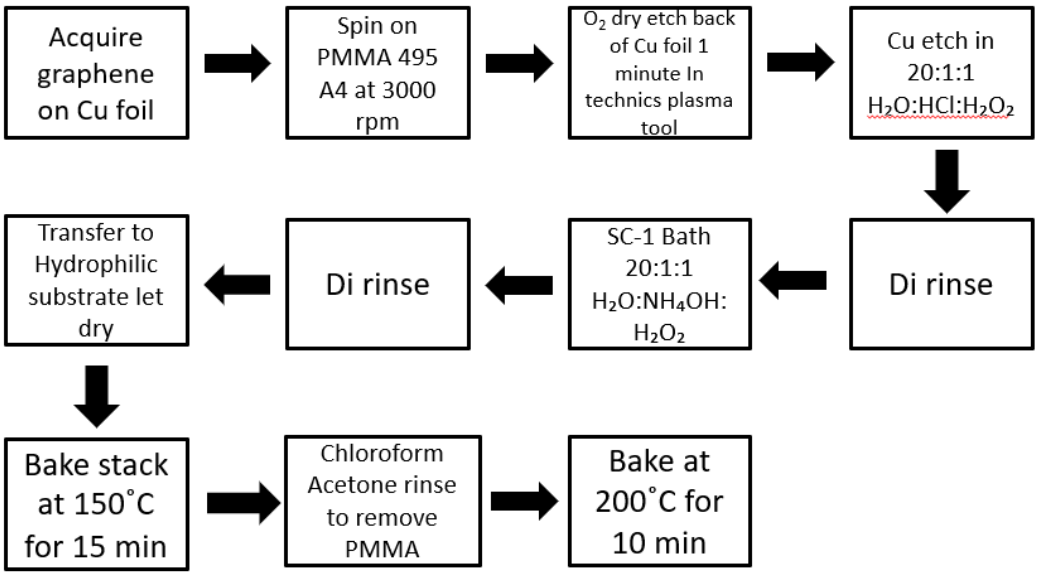

Figure 5.1: Process developed by the Graphene Supermarket in which graphene is transferred from a Cu foil to a substrate of ones choosing. Acetone rinse can be replaced with a chloroform rinse for better PMMA removal [44].

Liang et al. reported a successful transfer to the substrate with minimal defects in the graphene monolayer. Their results were attained through resonant Raman spectroscopy. It was found that the ratio of the disorder induced band (I_D), at a Raman shift of 1300 cm^{-1} and the Raman allowed band (I_G) in the graphene, did not increase significantly after the transfer process with the RCA clean. The standard process with no additional RCA steps did increase that ratio, which was an integrated 0.2 I_D/I_G. This allowed them to conclude

that the RCA clean steps do not increase, and in some cases, it can even decrease the defects in the graphene monolayer [44].

This transfer process is not the most efficient since it used high quantities of copper, which end up being disposed of and cannot translate to large production line processes for transfer graphene. Other groups have done significant work in an effort to reduce the waste and increase the processes scalability [45]. A good amount of research has gone into metal exfoliation of graphene for roll to roll transferring, *Zaretski et al.* published in 2015 their successful graphene transferring techniques. Their process relies on the preferential adhesion of graphene to different kinds of metals from a Cu foil. The group, PVD deposited nickle onto the graphene copper stack. Then, using a thermal release tape, the metalized graphene preferentially adhered to the nickle, and they transferred the stack to a polymer substrate [45]. The thermal release tape was removed and then the nickle was etched in an iron chloride bath [45].

The group then used Raman spectroscopy and sheet resistance measurements across the film to quantify the quality of the graphene monolayer [45]. They obtained a minimum sheet resistance of 163 Ω/sq, and compared that to the wet etch process minimum sheet resistance which was 325 Ω/sq[45]. They attributed this difference to metal doping of the graphene monolayer after the exfoliation process. There were also observable cracks in the nickle film due to the mechanical nature of the exfoliation process. These cracks will undoubtedly leave defects and topological features in the graphene monolayer [45]. When compared to that of the wet transfer process, the disorder peak to allowed peak ratios were smaller indicating that the wet transfer yields a more uniform and defect free monolayer of graphene[45].

6 Design and Fabrication of Graphene based THz Modulator

The device design and fabrication of the modulator followed a two-step series of processes to demonstrate process capabilities here at Rochester Institute of Technology and to ensure a working device. The first step was to run a transfer process done by this researcher using the available resources in the RIT Semiconductor Manufacturing and Fabrication Laboratory (SMFL). The second was to send a silicon/silicon dioxide substrate out to get an ideal graphene monolayer to better ensure device operation.

During the experimental work two different devices were made, a passive and an active modulator. The passive devices are comprised of the silicon substrate, a 300 nm silicon dioxide layer, a graphene monolayer, one transfer by the researcher and one transferred by the a company the specializes in graphene called the Graphene Supermarket. Following the monolayer, a second thin silicon dioxide layer, 50 nm thick, was deposited on top and a aluminum diffraction grating was patterned on top of that. This device was built to emulate that of Figure 4.2 and be a proof of concept that it will in fact absorb THz radiation.

Following the successful testing of the preliminary device, a active modulator was fabricated. This device contained a boron implanted well, which was covered by 300 nm of silicon dioxide, followed by the two forms of transferred graphene then the thin oxide dielectric layer. The metal grating was connected to pads for the application of a bias. This was realized by patterning contact cuts through the thick oxide to the implanted well underneath for a ground connection. The purpose of this device was to build an active modulator that absorbed a THz signal and could further modulate the total absorption.

The following sections describe the design, fabrication and testing details of the two different devices. Both devices were fabricated successfully and significant test results were obtained.

6.1 Device Designs

COMSOL simulations done by Dr. Jornet were obtained and evaluated for initial device design. Using the radio frequency and electro-magnetic waves physics module, it was shown that in a device that is comprised of a substrate, dielectric layer, a metal grating and a one dimensional boundary condition that was defined by the conductivity of graphene, surface plasmons could resonate at the terahertz frequency. The grating pitch ranged from 400 nm to 1800 nm and resulting wave propagation with varying intensities was achieved as seen in Figure 4.2.

Using this device design, a mask was made for the initial device consisting of 1000 nm lines with spacing's of 500, 1000, 1500, and 2000 nm apart as seen in Figure 6.1.

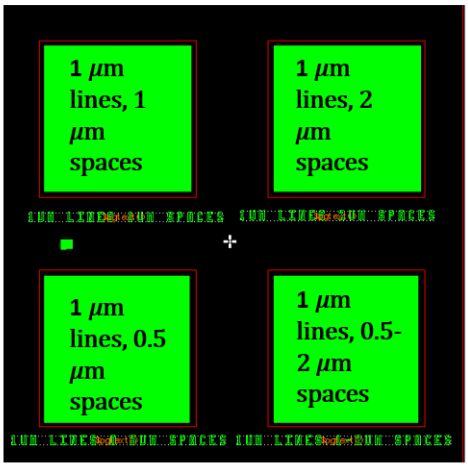

Figure 6.1: Designs of passive modulator. 1 μm lines and 1 μm spaces (top left), 1 μm lines and 2 μm spaces (top right). 1 μm lines and 0.5 μm spaces (bottom left). 1μm lines and 0.5, 1, 1.5, 2 μm spaces (bottom right) where each space increment covers 1 mm of distance.

This mask design for the preliminary device had two purposed. The first was to show that metal lines could in fact be patterned onto graphene without damage to the film or compromises to the structure. The second purpose was for a proof of concept that this structure could absorb THz radiation such that a THz signal could be modulated in the active modulator. The increase in SPP wave amplitude and on THz absorption was hoped to be evaluated by the differing pitches of lines on the mask as follows with the simulation results discussed in Chapter 4 by *Jornet et al.*. These results indicated an increase in SPP wave amplitude with decreasing pitch.

Once it was clear that the preliminary device could be made, the active device was designed and fabricated. The basic design of this device was based on the charge doping cross section shown in Figure 2.4. The reason for this was so that the graphene monolayer could undergo significant charge doping to modulate the absorption of the incoming THz signal. Figure (6.2a) shows the cross section of the designed device and Figure (6.2b) shows the layout of the device:

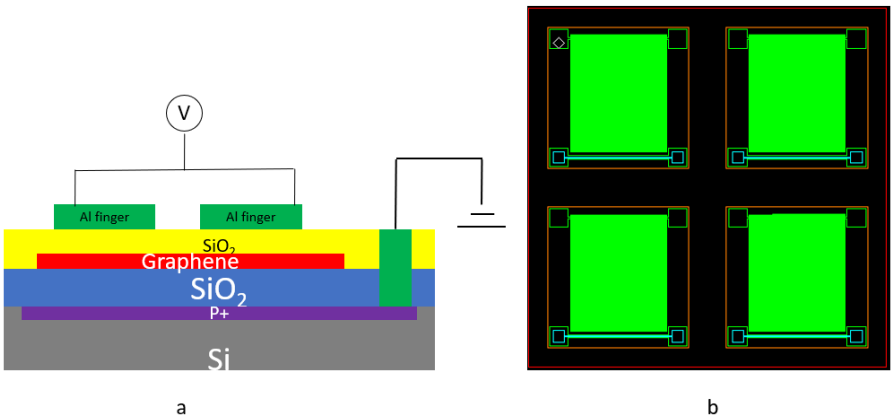

Figure 6.2: (a) Cross section of the active THz modulator in which a field will be applied across the metal, dielectric graphene stack to charge dope the graphene and modulate the amount of absorption of the THz signal. (b) Layout of active modulator.

Figure (6.2b) follows the same metal layout as Figure 6.1 except a contact connects all the metal finger at the top and resolves in a 500 x 500 μm pad. This design also has a contact cut (blue) to connect the metal to the P well (orange), which outlines the single active modulating devices. This layout also had to be a reduced size, such that the mask made could hold all three layers on a single plate. The layout die size was 9.5x9.5 mm and each individual device was 3.7 x 3.7 mm. This was a reduction from the single passive devices, which were 4.3 x 4.3 mm.

6.2 Fabrication of Passive and Active Modulators

6.2.1 Passive Modulator Fabrication

Two silicon 6 inch (100) orientation 5-10 Ω-cm p-type wafers were obtained and run through a standard RCA clean. Silicon dioxide was then thermally grown on the wafers in an oxygen ambient for 5 hours and 12 minutes at 1100 $^{\circ}C$. The wafers were then removed and the average oxide thickness was measured to be 3045 ± 15 Å. The purpose for this thickness is such that the graphene can be easily seen through a microscope due to the optical properties of SiO_2 at this thickness [44, 41, 45]. Figure 6.3 shows the cross section at this point.

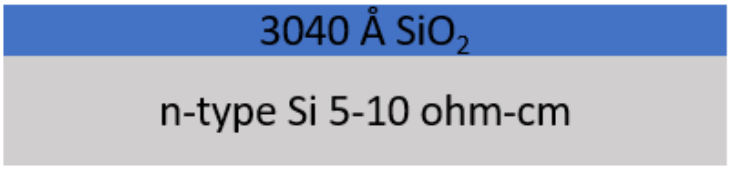

Figure 6.3: 304 nm of oxide grown in an O_2 ambient at 1100 ° on a n-type silicon substrate.

A graphene monolayer was then transferred on using a PMMA mediated RCA clean transfer technique [44]. Figure 6.4 shows the summary of the process steps for the transfer:

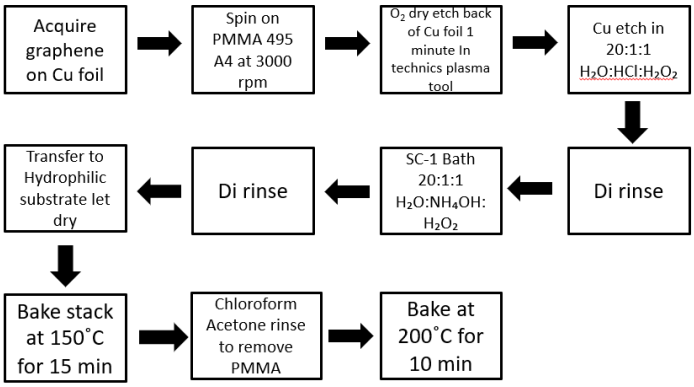

Figure 6.4: Process developed by the graphene supermarket and modified by the researcher to transfer a monolayer of graphene which minimizes the metal and organic contaminants as well as maintains the monolayer intact and reduces mechanical tears or cracks.

The details of this process are as follows. A 2x2 inch Cu foil with a monolayer of graphene was cut into 4 1x1 inch pieces. One of these 1x1 inch pieces was coated with 3 drops of PMMA at 3000 rpm. The Cu foil with graphene was taped on to a 6 inch silicon dummy wafer to ensure a proper coat as seen in Figure 6.5. Then, the sample was left to dry for one hour.

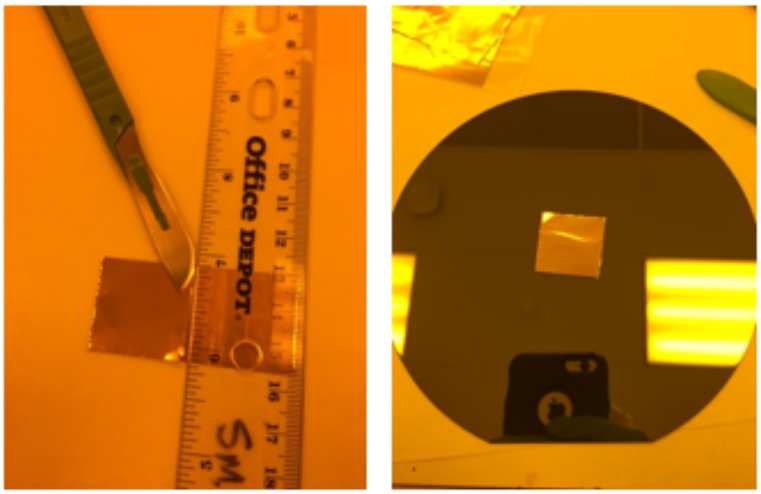

Figure 6.5: Cutting and PMMA coating of Graphene on a 1x1 inch copper foil.

The copper foil was then flipped over to expose its backside and re-taped to the same dummy wafer. Following this, the wafer with the Cu, graphene and PMMA foil was placed

in a Technics plasma asher for 1 minute at 200 W to remove the graphene that resided on the back of the foil.

To reduce folds or rips, chemical beakers needed to be filled up such that a 3 inch by 2 inch glass slide could be fully immersed into the solution. The graphene and PMMA stack, after etching, was placed such that it sat on top of the surface of the solution. Once the copper was fully etched away, a glass slide was immersed into the the solution close to perpendicular to the surface and aligned to promote the sticking of the graphene and PMMA film to the slide. Then the film can be transferred to a different solution or rinse beaker in a similar fashion. Figure 6.6 shows the sample of PMMA on top of graphene on a glass slide during such a transfer.

Figure 6.6: PMMA on graphene being transferred using glass slide method to maintain the integrity of the film.

During the first successful graphene transfer try, the Cu etchant used was a ratio 20:5:1 of H_2:HCl:H_2O_2, and the Cu was completely etched after 2 hours as shown in Figure 6.7 along with the ideal state of the sample.

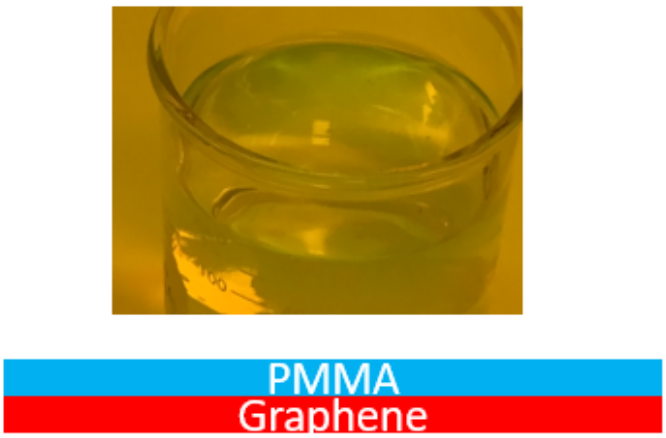

Figure 6.7: Picture of fully etch Cu foil and an idealized cross section of the sample.

Then, the sample was placed in a beaker of H_2O:NH_4:H_2O_2 to further clean the residual organic particles. Following this, a DI water bath was prepared and the Si/SiO_2 substrate was placed at the bottom of this bath. The 1x1 inch sample of PMMA and graphene was placed on the surface of the water. The wafer was then lifted to contain the sample in the center. When this happened, a thin layer of water resided on the surface of the substrate. The substrate was carried over to a bench and patted dry to further isolate and position the PMMA/graphene stack. Once the sample made contact with the substrate, the wafer with the sample was left to dry for 24 hours. Figure 6.8 shows steps within this process:

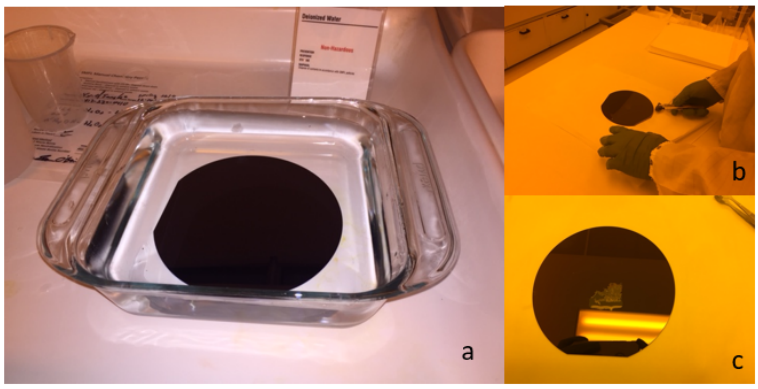

Figure 6.8: (a) Wafer sitting in DI water bath awaiting to be lifted out with PMMA/graphene stack on top. (b) Pat drying and manipulating wafer to position the PMMA/graphene sample in the center of the substrate. (c) Once contact between substrate and sample was made, it was left to dry for 24 hours.

After air drying, a bake was done to further remove any residual moisture at 150 °C for 15 minutes. The PMMA was then dissolved in acetone. For the PMMA dissoltuon often times chloroform is used for a more complete dissolution [44], however, chloroform was unavailable at this time. After the PMMA dissolution another bake was done at 200°C for 10 minutes to adhere the graphene to the SiO_2 and pictures were taken of it as seen in Figure 6.9

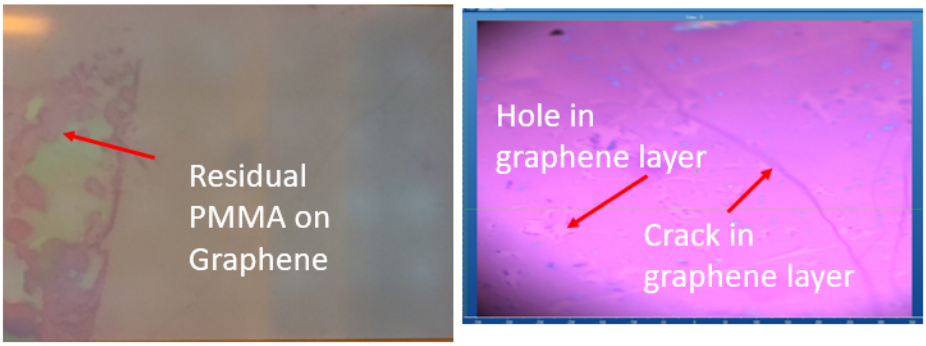

Figure 6.9: Pictures of transferred graphene with residual undissolved PMMA (left) and holes and cracks from the aggressive etch and further processing (right).

From the examination of the film, it was clear that the etchant was too strong and too fast, which lead to holes and tears in the graphene monolayer.

At this point Raman spectroscopy was done to confirm the successful transfer of the

graphene. The Raman spectra consist of the two characteristic peaks G and G'. These were first observed on a control sample consisting of a glass slide with a graphene monolayer that was purchased from Graphene Supermarket. Raman spectra attained at RIT of that glass slide was compared to that of the graphene transferred by the researcher in the RIT SMFL, the results can be seen below in Figure 6.10. In the spot where the Raman spectra was taken, it is clear that it is no longer a monolayer in that location. The G:G' peaks is 1:1 and this is indicative of a bi-layer of graphene [46]. This was most likely caused by a wrinkle during the transfer process [46].

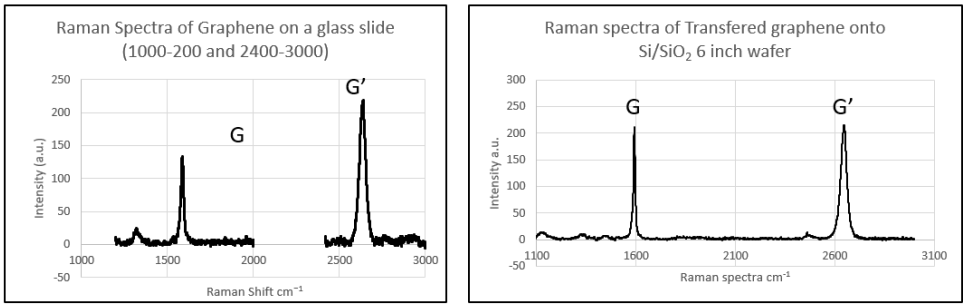

Figure 6.10: Results of Raman spectra of graphene on a glass slide (left), results of Raman spectra attained on graphene transferred at RIT (right).

After the transfer and the confirmation by Raman spectra, a 50 nm silicon dioxide film was deposited through a Tetraethyl orthosilicate (TEOS) plasma enhanced chemical vapor deposition (PECVD) process. This was done on the AME P500 PECVD tool. The recipe used was A6-1KA TEOS LS and the deposition time was reduced to six seconds to obtain 50 nm of oxide.

6.2.2 Lift off Lithography

Following the deposition of the oxide, metal lines were patterned via lift off lithography. This was done by coating an lift off resist (LOR). Followed by the coating of a standard

lithographic i-line resist, MiR 701 photoresist, and exposing it on an ASML stepper. Then, the pattern was resolved with the standard chemical developer CD-26. After this, metal was deposited on top and an ultrasonic bath of N-Methyl Pyrrolidinone (NMP) was used to dissolve the LOR resist and leave behind the metal lines, which sat atop of the deposited oxide.

LOR is a common positive resist used for lift off processes. The active ingredient is cyclopentanone and quickly dissolves in standard lithographic developers [47]. LOR resist is also very dependant on its soft bake temperature. High soft bake temperature yields a much slower dissolution rate in CD-26 because of its glass transition phase which is around 190°C [47]. Therefore a longer soft bake at this high temperature was found to yield the best results.

LOR 5A does not have a photoactive chemical therefore there is no preferential dissolution after exposure. Once immersed in a developer, it will dissolve isotropically. Because of this, for small features, a fast spin speed was necessary to achieve a thin layer. This way, it can maintain the structure of small features for the lift off material. These features will be defined by the patterned photoresist which sits on top of the LOR 5A. The stack was also exposed with a reduced dose of 160 mJ/cm^2 which was optimized for this process with an exposure matrix. The standard post exposure bake temperature and time was increased to 120 °C and 1.5 minutes, and the development time was reduced to 30 seconds as opposed to 45 seconds all to reduce LOR dissolution. Figure 6.11 shows the lift off process with LOR:

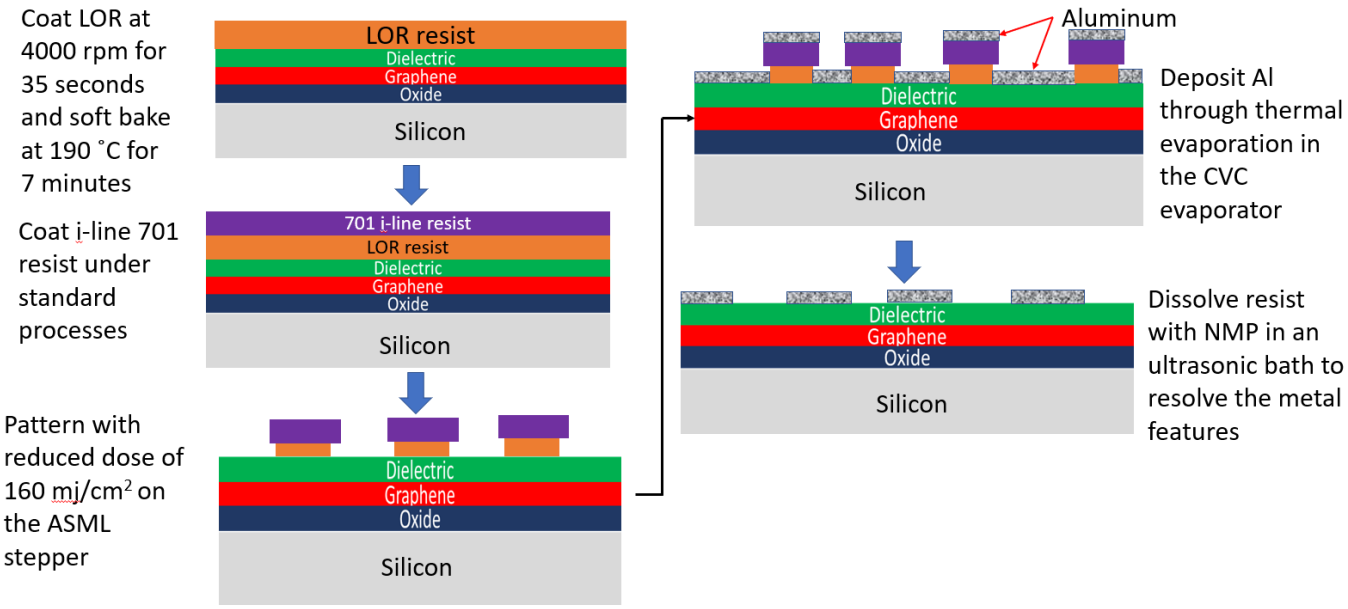

Figure 6.11: The full lift off process with LOR resist.

For the lift off process run, LOR 5A was coated onto the wafer at 4000 rpm for 35 seconds. Following this it was baked at 190 °C for 7 minutes. Then 701 photoresist was coated with the wafer track at 3500 rpm. No HMDS was used for the 701 coat nor was a dehydration bake done. A soft bake was done at 95 °C for 1 minute. The wafer was then exposed on the ASML with the reduced dose of 160 mJ/cm^2. Then, a post exposure bake was done for 1.5 minutes at 120 °C. It was then developed on the wafer track for a reduced develop time of 35 seconds and a reduced rinse time of 10 seconds. No hard bake was done.

The purpose for the reduced develop time and no hard bake was so that the T shaped structures shown in Figure 6.11 could be realized. To complete the lift off, Aluminum was evaporated on the CVC evaporator for 3 minutes at a thickness that did not go beyond the LOR layer as shown in the last steps of Figure 6.11. The thickness of the Al, as measured by the Inficon film thickness monitor, was 210 nm. This thickness monitor worked through a vibrating crystal which had to be calibrated to zero for every run. This thin Al deposition

allowed the lift off solvent to reach and dissolve the LOR to properly resolve the image.

Figure (6.12a) shows the metal lines being resolved on the preliminary device in the ultrasonics bath and Figure (6.12b,c) shows the result of the Al lines on top of graphene:

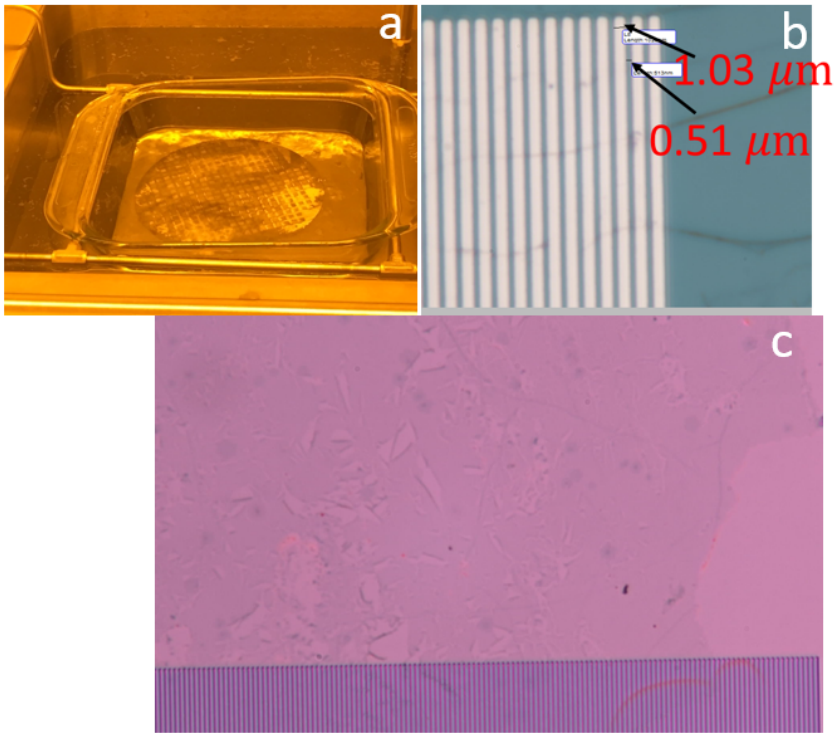

Figure 6.12: (a) Aluminum being lifted off the wafer in an ultrasonics bath of NMP. (b) zoomed in picture of 1000 nm aluminum lines with 510 nm spaces. (c) Zoomed out picture of aluminum lines showing graphene underneath.

During the fabrication of these devices a few complication arose. One of the most significant was that during the lift off process, significant damage occurred to the thin oxide layer atop of the graphene monolayer. This resulted in the oxide coming off and significantly reducing the yield of functional devices. This damage was only localized to the areas with continuous graphene. Figure 6.13 shows this resulting damage

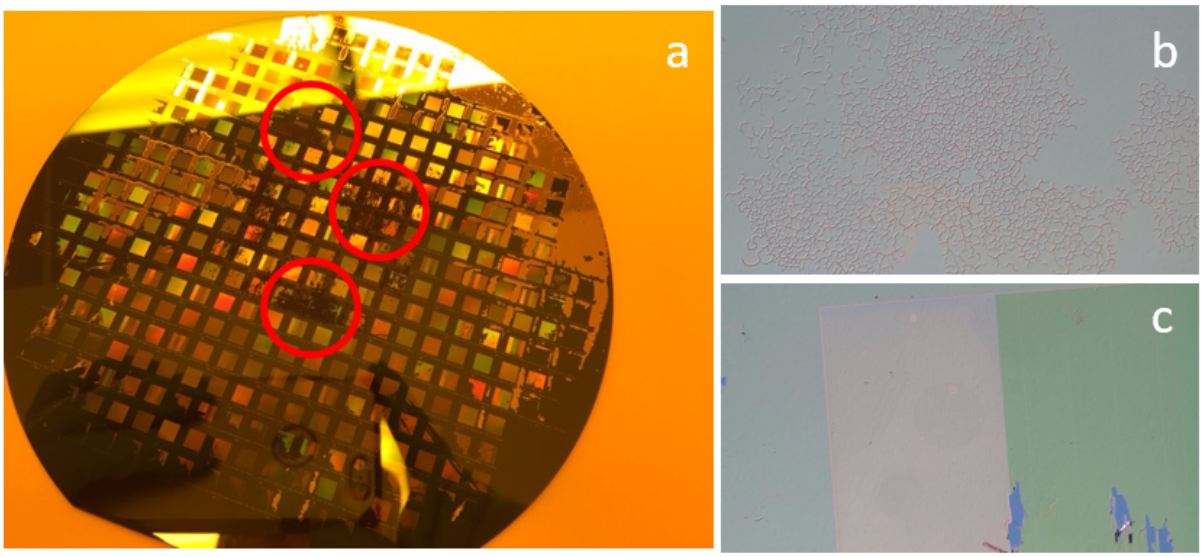

Figure 6.13: (a) View of full wafer and areas in which the oxide came up removing the metal lines that were on top. (b,c) zoomed in pictures of thin oxide cracking and metal line damage due to its cracking.

It is believed that this damage came from water being trapped between the graphene and thin oxide layer due to the hydrophilicity of silicon dioxide. This led to stresses in the thin oxide and its inevitable cracks and breaking. Thus, very few of the passive modulator devices were tested. To preserve the devices with graphene, a complete lift off of the Al was not done as can be seen by the residual Al in Figure 6.13. Further research was done in hopes to remedy this problem and solutions were found and applied during the active modulator fabrication.

6.2.3 Active Modulator Fabrication

Two silicon 6 inch (100) orientation 5-10 Ω-cm p-type wafers were obtained and run through a standard RCA clean. Then the wafers were patterned with standard RIT SMFL i-line lithographic techniques to define alignment marks for the lithographic levels described as

follows. HMDS primer was vapor deposited at 140 °C followed by a coating of 701 resist on the wafer track. The wafer was then soft baked at 95 °C and exposed on the ASML with the level 0 alignment job with a dose of 275 mJ/cm^2. The wafer went under a post exposure bake of 110 °C and the marks were developed on the wafer track and hard baked for 1 minute at 125 °C. This was followed by a Trion Phantom RIE etcher was used to etch the pattern into the silicon with the SMFL poly-silicon recipe of 50 sccm of SF_6 and 9 sccm of O_2 for 1 minute at 125W and a pressure of 100 mTorr.

The resist was then removed by a O_2 plasma asher and the wafer was once again coated with photoresist and ran through standard i-line lithographic techniques, as described in the previous paragraph, to pattern the wafer for the diffusion level using the SANCHEZactivemod job and the SANCHEZ-THz reticle. After the diffusion wells were resolved, a Varian 350D Implanter was used to implant B11 ions at a dose of $1x10^{15}$ cm^{-2} at an energy of 50 KeV and a implant current of 50 μAmps. This was done such that ohmic contact could be achieved between the implanted area and the contacting metal. The low implant energy was used to not implant through the resist and a low current was used to not burn or damage the masking resist.

Following the implant a piranha clean was used to remove the implanted resist. The wafer was then RCA cleaned and placed in the Bruce furnace tube 4 to grow 300 nm of oxide in an O_2 ambient for 5 hours at 1100 °C. Following the oxide growth, one wafer was mailed to Graphene Supermarket for a graphene transfer and the other went through the graphene transfer process developed at RIT.

Graphene on a 1x1 inch Cu foil was obtained and coated with PMMA at 3000 rpm. The PMMA was left to dry for one hour with no hard bake. The sample was then placed

upside down in the Technics plasma etcher for 1 minute with 20 sccm of oxygen at a power of 200W and a pressure of 100 mTorr to remove any graphene on the backside of the Cu foil. Following this step, the Cu was etched in a solution of 20:1:1 H_2O:HCl:H_2O_2 overnight. This was a diluted etchant as compared to the first graphene transfer try described in the previous section. The purpose for this was to achieve a slower and gentler etch as to limit the amount of damage to the graphene monolayer. The Cu was fully etched away and the sample floated atop the surface of the solution as shown in Figure 6.14.

Figure 6.14: Graphene and PMMA stack floating along the surface of the Cu etchant. Blue tinge in solution is the dissolved Cu from the Cu foil.

Following the etch, the sample followed the same steps as that of the original transfer outlined in Figure 6.4. After the chloroform bath, pictures were taken of the resulting graphene transfer. These can be seen in Figure 6.15

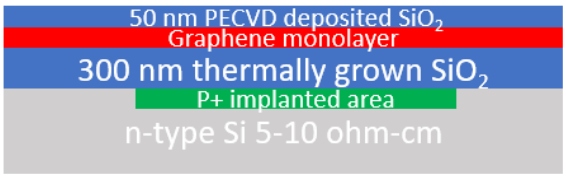

Figure 6.16: Cross sectional view of the device after the deposition of the thin silicon dioxide.

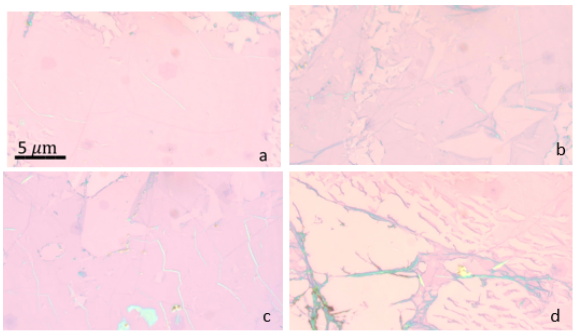

Figure 6.15: Pictures resulting from the 2nd successful graphene try of various continuities of the graphene monolayer film.

It was very apparent that this transfer was much more successful compared to that of the first successful attempt. This is largely due to the use of chloroform to remove residual PMMA and the less aggressive etchant used to etch the copper foil. Figured 6.15d shows the worst area of the transfer while Figures 6.15(a,b,c) show what the majority of the films looked like.

After the transfer, 50 nm of silicon dioxide was deposited through a low stress TEOS PECVD process for 6 seconds using the same recipe used for the passive modulator device. The wafer was then put into the Bruce furnace tube 5 to be densified for 2 hours at 600 °C in a nitrogen ambient of 60 sccm of N_2. At this point, the wafer cross section is shown in Figure 6.16

The wafer was removed and the thickness of the total oxide was 360 nm. The wafer was then patterned using standard i-line lithographic process steps as described above. The

SANCHEZactivemod job along with the SANCHEZ-THZ mask were used to pattern the contact cuts (CC) using the contact cut level mask. The CC oxide was then etched in the Trion minilock under the following conditions outlined by Table 2:

Parameter	Value
CHF_3	60 sccm
CF_4	30 sccm
Ar	50 sccm
O_2	10 sccm
Power	100 W
Pressure	100 mTorr
Time	8 minutes

Table 2: Parameters used during Trion etch developed by the researcher at RIT.

The etch rate of this recipe was found to be 30 nm/min. Following the CC etch, the wafer had to be ashed to remove the plasma exposed resist. The results of the CC level etch and a cross-section of the device up to this point are shown in Figure 6.17.

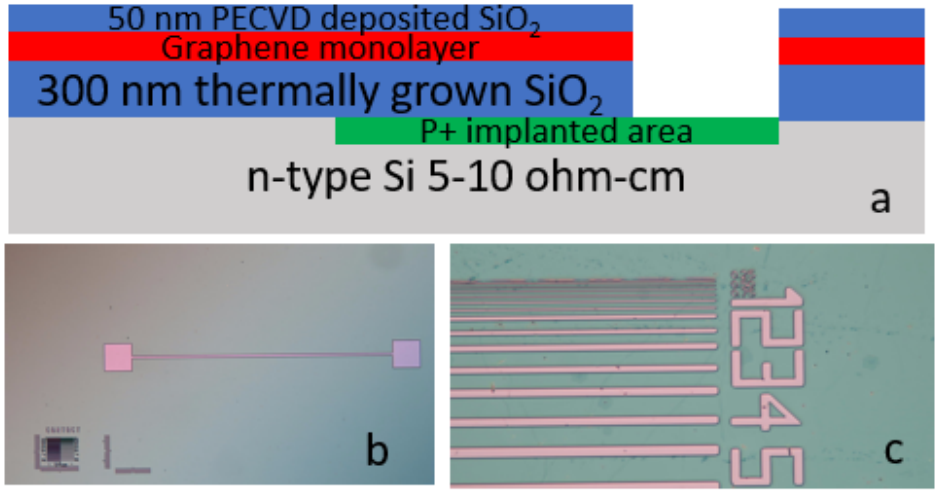

Figure 6.17: (a) cross section of device at this point. (b) resulting CC etched area. (c) Resulting lithographic vernier such that minimum resolution is 1000 nm and graphene underneath can be seen to have survived the process steps.

Once the CC areas were defined, the metal lift off process developed for the preliminary device was used to complete the fabrication of the device. Metal was evaporated at a base pressure of 6.5x10^{-7} Torr. Then it was placed in an ultrasonics bath of Baker PRS 2000. This was a different solvent than used for the Preliminary device which was Remover PG. The results of this can be seen in Figure 6.18. Little to no damage to the thin oxide was apparent, much of this had to do with the densification step.

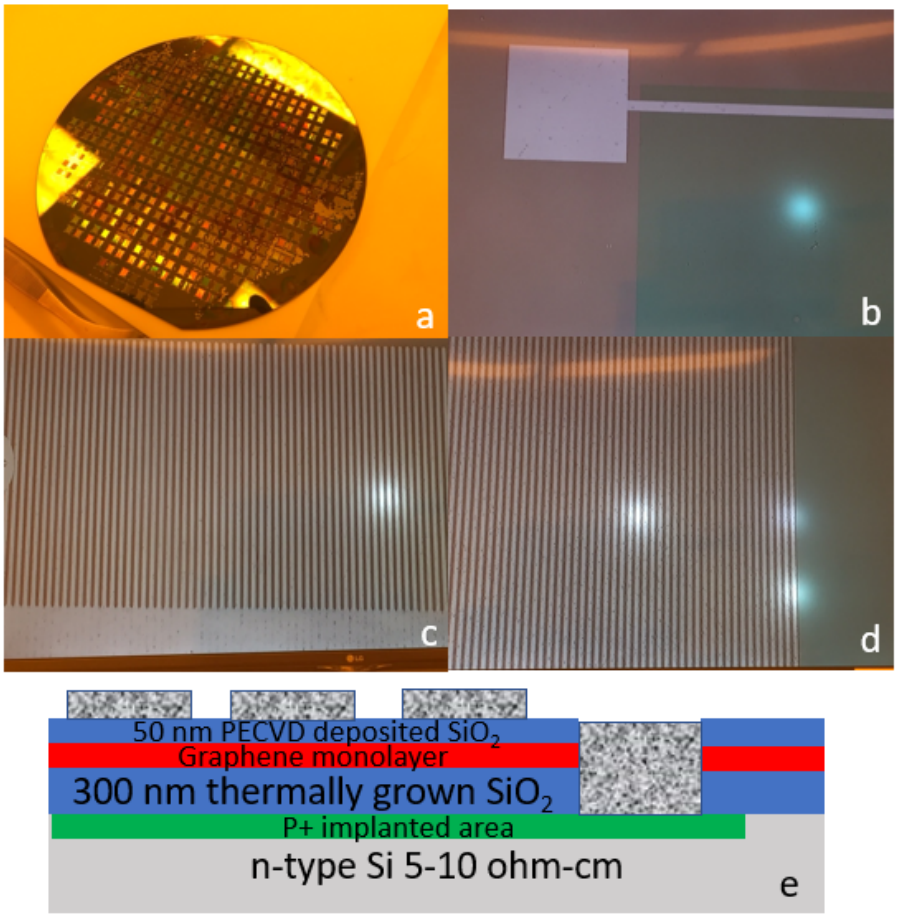

Figure 6.18: (a) Entire wafer with finalized devices. (b) Connecting Al pads to Al lines for the application of a bias. (c) 1000 nm Al lines coming from the connecting metal. (d) Al lines over graphene. (e) Cross section of entire device.

From Figure 6.18 (c,d) the metal lift off process step was not of the same quality as that of the preliminary device seen in Figure 6.12 (b). The lines for this lift off step yielded some

damage and pitting. This could be due to the higher base pressure of 6.5x10^{-7} Torr in which the Al was evaporated at. This compared to the base pressure of 3x10^{-7} Torr is substantially larger. A higher base pressure can cause an increase in contaminants during the evaporation process which can be embedded in the Al film. Then, when exposed to the solvent, and the mechanical motion of the ultrasonics bath, these contaminates can come off the Al lines and leave behind pits and other damage.

At this point, the wafer was taken to the wafer saw and sawed in steps of 10.5 mm following that of the lithographic dies. Therefore each chip had a total of four devices on it where each device had the varying spaces between the Al lines. However, there was extensive damage done to the metal lines due to particulates crashing into areas of metal lines and causing significant scratches. Figure 6.19 shows the results of the wafer sawing and resulting damage.

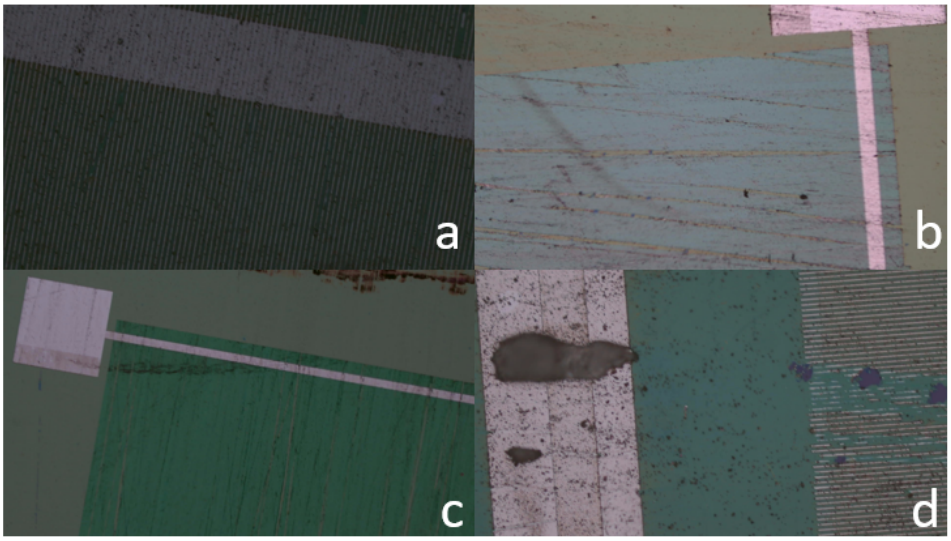

Figure 6.19: Images of the scratched wafers of various degrees after the wafer saw step.

Due to how the device was designed, all Al lines connected to the pads will still emit the modulating bias. As shown in Figure 6.19(a,c), the majority of the lines are still connected

to the pads. The scratches seen are severe, however the metal can still apply the modulating bias across the majority of the devices. With a comparison between Figures 6.19 and Figures 6.18, further research is clearly needed to protect the Al lines from damage during the dicing and packaging stages of the process. As seen by the purple shapes in Figure 6.19(d) there is still some lift off of the thin silicon dioxide in areas where there were no metal lines.

6.2.4 Active Modulator Packaging

The final part of fabrication was the device packaging. This part is what enables us to successfully test individual devices such that single device operation can be realized. Figure 6.20 shows the PCB board with the designed copper lines.

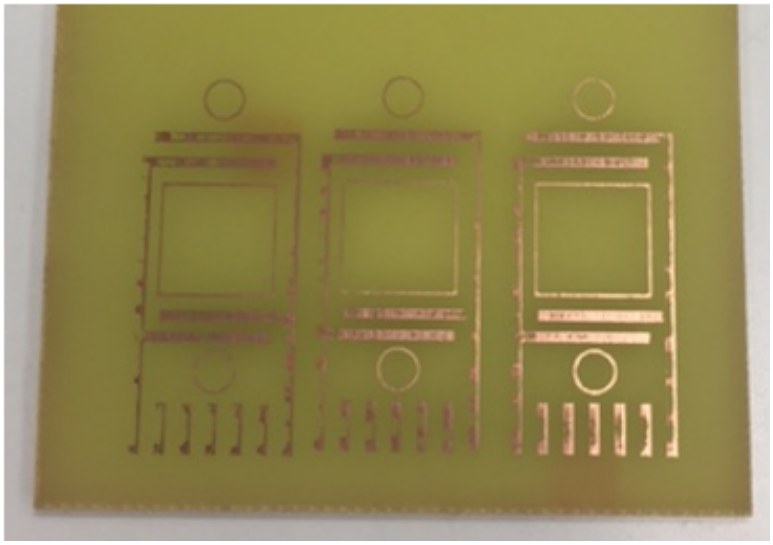

Figure 6.20: The three PCB boards used for wire-bonding in which connects all four devices to the same ground and bias connections.

Figure 6.20 was built such that single devices or the entire chip can be modulated at one time. As will be described in the testing of the passive device, spatial constrictions were encountered such that only entire chips could be illuminated. Therefore, this packaging set up was done so that if the same area constrictions are encountered, the entire chip can

be biased. If there is no spatial constriction, then each single device can be illuminated separately and the bias can still be applied.

A PCB board with copper was obtained and coated with HPR 504 resist at 1500 rpm for 60 seconds. Then it was soft baked at 100 °C for 4 minutes. The PCB board design was printed on a transparency and placed on top of the sample and covered with a glass plate to flatten it. The sample was flood exposed with the Karl Suss MA150 tool for 20 seconds, which is equivalent to a dose of 200 mJ/cm^2. The sample was then developed in CD-26 for 1 minute.

The resist was hard baked at 140 °C and the copper was etched in a mixture of H_2O:HCl:H_2O_2 3:1:2. After a complete etch, the resist was stripped in acetone and then rinsed in DI water. Once the PCB boards were made, the chip was glued on to the designated area and wire bonded with Al wire bonds. Figure 6.21 shows the packaged device along with a magnified view of the wire-bonding process. Electrical male pins were soldered to the corresponding pads on the PCB board such that wires could be connected to apply the positive bias and ground the device.

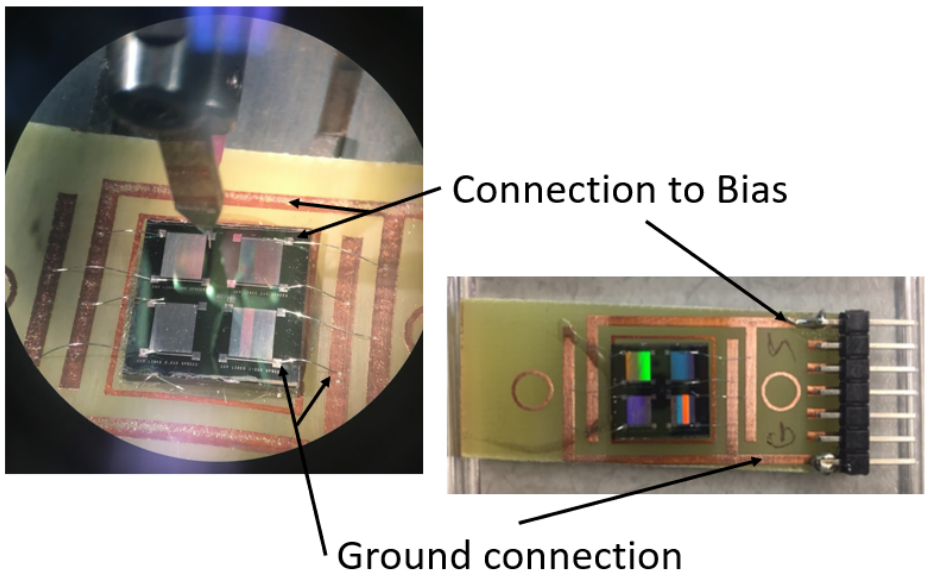

Figure 6.21: Fully packaged device (right). Magnified view of wire-bonding pads to the ground and bias connections (left).

7 Graphene Based THz Modulator Testing and Results

This chapter discusses the test set up used and the results obtained for both the passive and active modulators. For both devices, only the devices with the Graphene Supermarket transferred graphene monolayer were tested. This was done to verify that, in the case of little or no THz absorption, the fault would be in the fundamental design of the device and not due to discontinuities or damage in an experimentally transferred graphene monolayer. With the use of the Graphene Supermarket transferred graphene, it is assumed that the best transfer was obtained and the fault is in the device design or a different process step in the device fabrication.

7.1 Passive Device Testing

The passive device was tested with the help of the University at Buffalo center for THz Communications. A 1.00 THz source with a power of 30 μWatts and a receiver were set up 5 cm away from the wafer as shown in Figure 7.1. The purpose of the set up was to measure the reflected power and to determine the attenuation of the signal on different surfaces. The receiver was an oscilloscope that measured the reflected signal from the wafer. Since most electrical systems, including the oscilloscope used, cannot operate at THz frequencies, the reflected signal had to be down converted and recovered at 500 MHz. This would confirm the absorption of the THz signal.

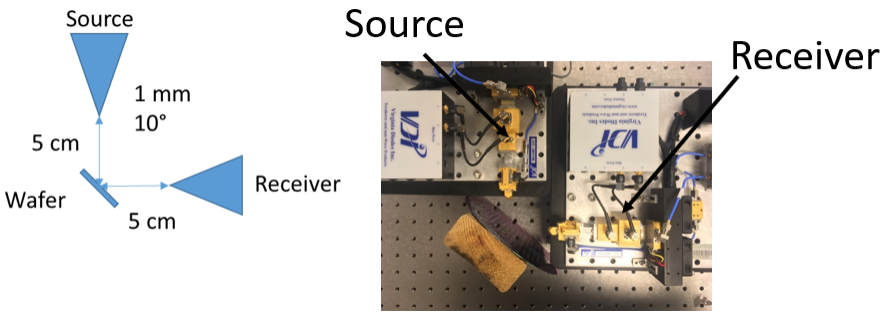

Figure 7.1: The experimental set up used to test the preliminary THz modulator.

With a beam width of 1 mm and a spread of 10°, the devices were illuminated by a 10 mm diameter beam when placed 5 cm away. The wafer could not be placed closer due to spatial restrictions of the test set up. Due to these spatial restrictions, the expected beam width of 10 mm is shown in Figure 7.2. Therefore, the measured results were an average of areas with and without Al grating over the graphene monolayer. The passive modulator, Al grating without graphene and blank silicon dioxide were illuminated with the 1 THz source and the reflected signal was measured.

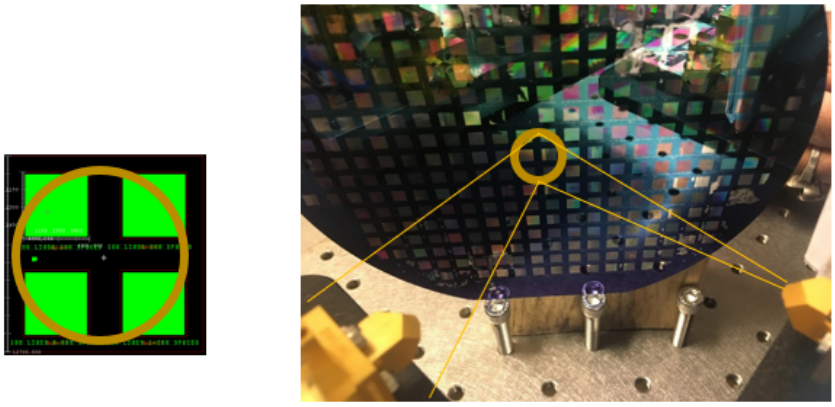

Figure 7.2: The illumination of the passive THz modulator.

Figure 7.3 shows the devices tested.

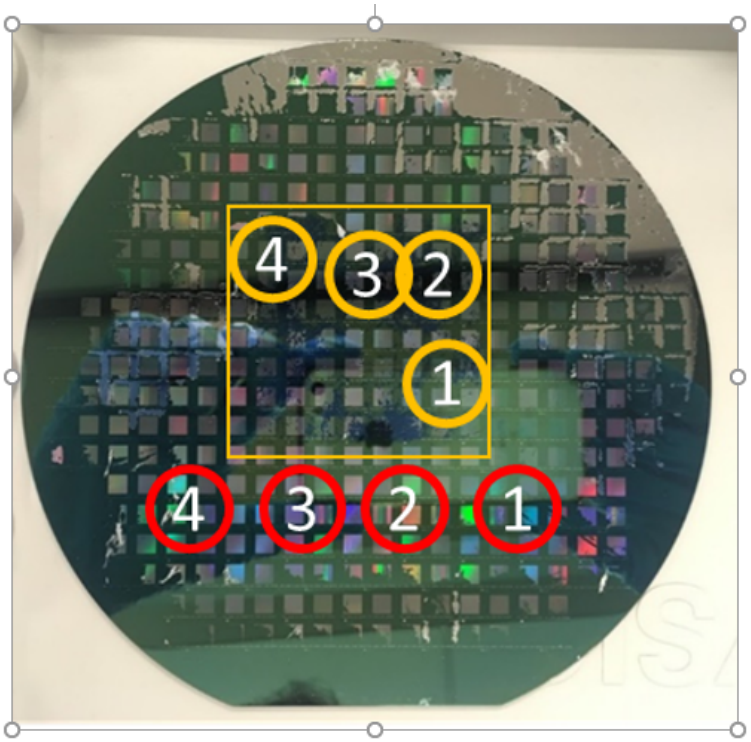

Figure 7.3: Devices with Al grating and graphene underneath (orange). Devices with Al grating and no graphene underneath (red).

In Figure 7.3 the graphene monolayer is outlined by the yellow box. As seen in the surrounding areas of the yellow box, the devices with no graphene underneath experience minimal damage from the thin oxide lift off (red circles), unlike those with graphene (yellow circles).

7.1.1 Passive Device Results

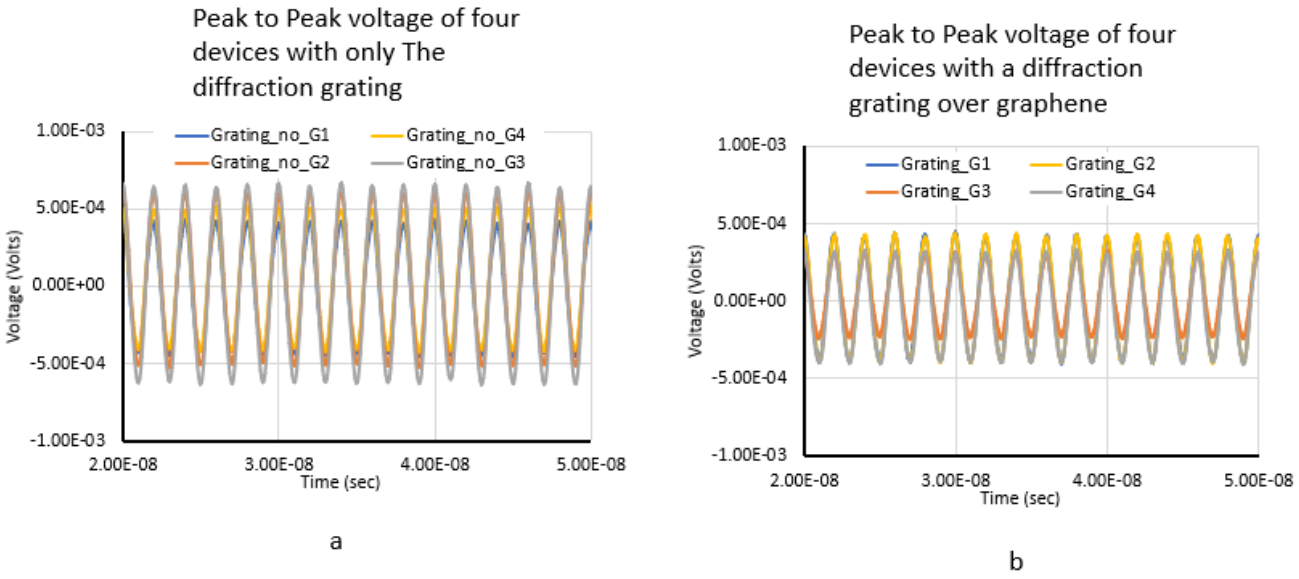

Figure 7.4: Oscilloscope data of voltages of device area with and without graphene.

From the tests run at the University at Buffalo, a total of 50% reduction of the incident power was attained as an average of reflected signal between grated and not grated graphene. Figure 7.4 (a,b) shows the actual oscilloscope data of the reflected signal of just an Al grating Al grating over silicon dioxide (a) and Al grating over silicon dioxide and graphene (b). These can be compared to received signal of bare silicon dioxide as shown by Figure 7.5.

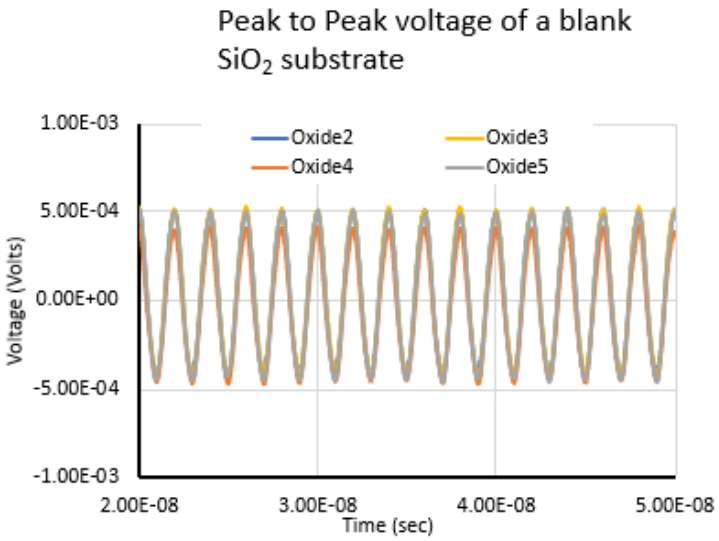

Figure 7.5: Oscilloscope data of voltages of areas with bare silicon dioxide.

Figure 7.6 shows the average peak to peak value. By the difference in average peak to peak voltage, the presence of the graphene increases the absorption of the terahertz signal.

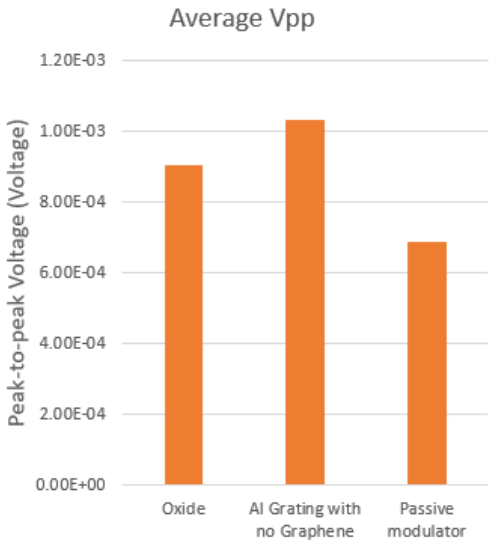

Figure 7.6: The average peak to peak voltage of four areas with graphene, without graphene and just oxide.

Peak to peak voltages were calculated from the data recorded by the oscilloscope. These

peak to peak voltages are measurements of the amplitude of the reflected signal. In Figure 7.4, the device without graphene has a peak to peak voltage of 1.05 mV +/- 0.2mV where as the device with graphene has 0.65 mV +/- 0.2 mV.

From the results it can be argued that significant THz absorption occurred with in the presence of graphene. Shown by the 0.4 mV reduction in amplitude of the signal between Figure 7.4 (a) and Figure 7.4 (b). It is important to note that the lowest amplitude found of the device with no graphene is of the same order as that of the highest amplitude found with graphene. Statistically speaking, there is a clear trend, however, a conclusive statement cannot be made about the degree of THz absorption in these passive devices.

The absorption compared to that of the theoretical development of the graphene grating solution [13] is much higher than anticipated. The theoretical calculations done by *Peres et. al.* calculated a maximum 45% absorption of the THz signal in cases where the grating height was double the size of the grating pitch [13]. Figure 7.6 results were obtained from a chip in which the minimum grating pitch is 1500 nm and a grating height of 210 nm. The measured 50% absorption of the signal from this device is greater than that of the calculated value, which was 45% signal absorption. This difference is accentuated by the fact that the grating thickness to grating width ratio is far from the maximum of 2:1 as calculated by reference [13]. However, due to the fact that there is some absorption of THz radiation by the oxide as well as absorption by the Al grating with no graphene as shown in Figure 7.6, it would be expected that these values will be larger than a theorized grating over an ideal graphene monolayer.

With an already well transferred graphene monolayer, SPP wave propagation at the THz frequency has been repeatedly reported and confirmed as described in Chapter 4. It has also

been confirmed that the graphene plasmons can absorb THz radiation as discussed by [1, 13] and experimentally confirmed by [5, 29]. Thus, results stated above were expected since the measurement of THz absorption has been well documented.

The presence of SiO_2 with graphene has also been discussed and reported on [5, 27, 29]. In reference [27], some analysis was given to the electrodynamics of a graphene-SiO_2 interface. In their near field amplitude experiments, they report a high amplitude increase of radiation at near to far IR wavelengths. As well as a much larger contribution of graphene's Drude-like conductivity than theorized with the presence of SiO_2 [27]. Therefore, with the designed device and the inclusion of SiO_2, it was further expected that the propagation of SPP waves and absorption of a THz signal will be enhanced.

The initial devices designed for THz absorption and modulation described by Dyakonov and Shur shallow water analogy [4], as well as the solution to the grating over graphene [13], informed much of the device design and operation. These initial designs were used for both the simulations run by Dr. Jornet [12] and the device structure used in this work. The Dyakonov and Shur shallow water analogy required high mobility and high electron density semiconductors such that there was no damping of the plasmonic wave, but there was a dense enough 2DEG to propagate actual plasmons [4]. These characteristics are found almost exclusively in semi-metals that follow the classical Drude-like conductivity [4, 12, 32]. Graphenes' conductivity has been modeled and experimentally confirmed to have this Drude-like conductivity at room temperature and, without any doping, matches that of the characteristics described by the shallow water analogy [9, 12, 20, 29].

Many of the structures reviewed in section 4.2 used the transmission of a THz signal through a 2DEG and then attempted to modulate that signal through the depletion or

accumulation of electrons. Significant results were obtained. However, the application of such a device is difficult since that modulated signal still needs to be directed to other places. Since this passive modulator achieved significant THz absorption, SPP wave resonance can be inferred because of its previous experimental confirmation in graphene based devices [5, 27, 28], it is much more practical for communications. The signal can be better directed once resonating in the device structure and has the potential to dynamically modulate pulsed THz signals.

7.2 Active Modulator Testing

Active modulators were diced and separated by the lithographically defined dies such that single devices could be illuminated during the testing. These devices were then wire bonded to a PCB board in the following device packaging model shown in Figure 7.7.

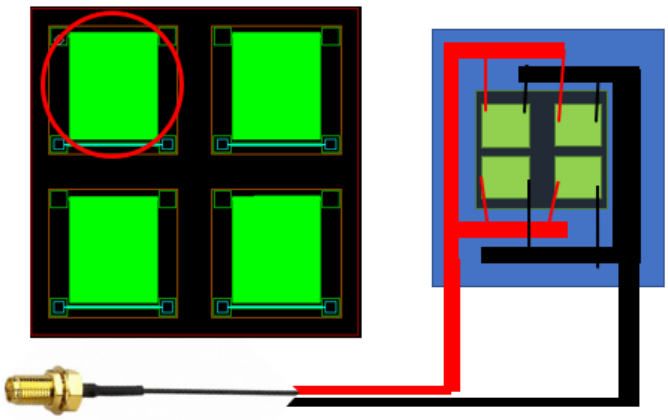

Figure 7.7: Wiring of the active modulator such that a voltage can be applied to the metal fingers (red) and a ground connection can be connected (black) which will be connected to a SMA cable (right). This set up and packaging also enables a smaller illumination ring such that single devices can be illuminated by the THz source (left).

This device packaging will enable the researchers to better quantify the effect of varying grating pitch, as well obtain direct data of device operation as opposed to the averages over

lithographic dies, since the chips can be placed closer to the source. The modulation was measured by the comparison of the reflected power at varying applied voltages. Figure 7.8 shows the test set up for the 1 μm line and 1μm spaces:

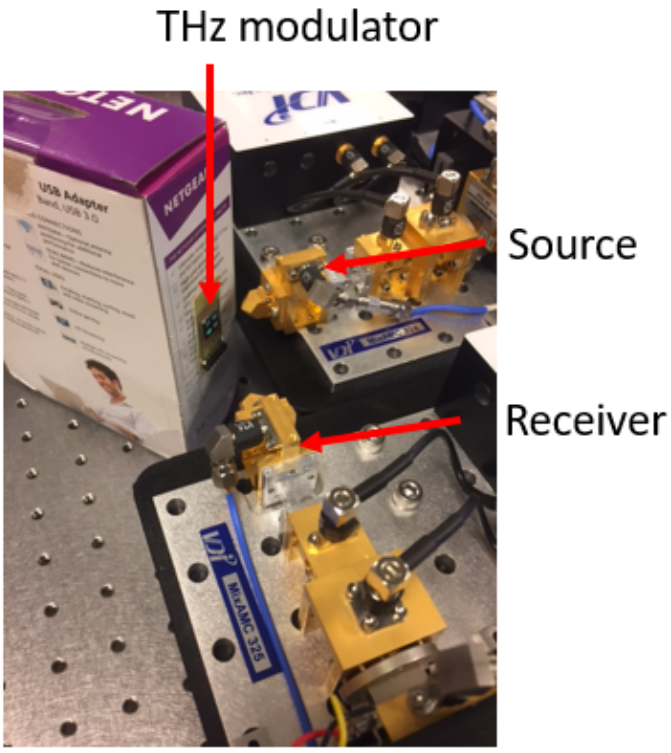

Figure 7.8: Test set up used for the active modulator in which a 1 THz pulse was directed at the THz modulator and then the reflected power was measured by the receiver.

The incoming 1 THz signal at 15 μWatts power was down converted to a 500 MHz signal and recorded on an oscilloscope. DC biases of 0 V, 1 V, 2 V, 3 V, 5 V, 6 V, 9 V then 12 V were applied and the reflected signal was measured. After the application of the 12V bias, a negative bias was applied to further explore its operation. A bias of 0 V was applied first to set a reference. Then, negative bias steps of -3 V, -6 V, -9 V, and -12 V were applied. Afterwards, to further confirm continuous operation, biases of 0 V, 12 V and then 24 V were applied and the reflected signal was measured.

7.2.1 Active Modulator Results

After the testing of the active modulator, the reflected signal was measured by an oscilloscope and the data was recorded and plotted as shown in Figure 7.9.

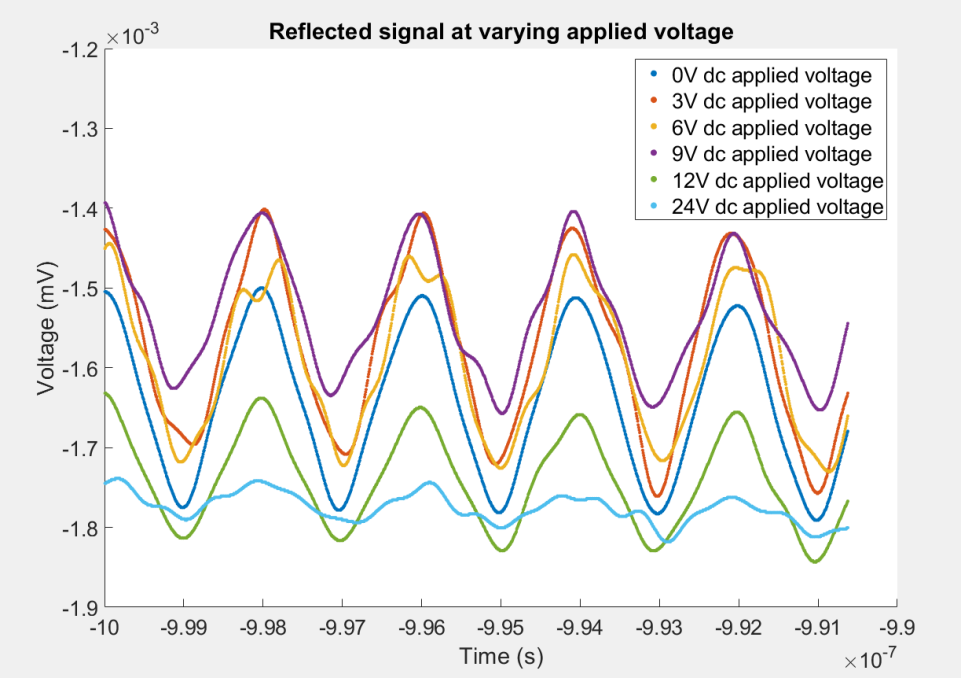

Figure 7.9: 500 MHz wave of the down converted reflected signal from the THz modulator at applied biases of 0 V, 3 V, 6 V, 9 V, 12 V and 24 V.

Modulation can be seen in Figure 7.9 by the reduction of amplitudes between each voltage step of 0 V, 3 V, 6 V, 9 V, 12 V and 24 V. At a bias of 24 V, most if not all of the THz signal was absorbed by the device. The received amplitudes measured V_r can be converted into gain, dBm and dB values using the incident signal amplitude V_0 which was 27.38 mV, the circuit impedance Z which was 50 Ω and equations 7.1-7.4 listed below.

$$Gain = \frac{V_r}{V_0} \tag{7.1}$$

$$dB = 20log(\frac{V_r}{V_0}) \tag{7.2}$$

$$dBm = log(\frac{P_r}{1mW}) \tag{7.3}$$

$$P_r = \sqrt{V_r Z} \tag{7.4}$$

Table 3 shows the values calculated with the application of 0 V, 9 V, 12 V and 24 V bias.

Bias	Received Amplitude (Vr)	Gain (Vr/Vo)	dB	dBm
0 V	0.125 mV	4.56×10^{-3}	-46.82	-65.05
9 V	0.110 mV	4.01×10^{-3}	-47.94	-66.16
12 V	0.080 mV	2.92×10^{-3}	-50.69	-68.93
24 V	0.020 mV	0.73×10^{-3}	-62.72	-80.95

Table 3: Received signal amplitude and the calculated gain, dB and dBm for the given applied biases of 0 V, 9 V, 12 V and 24 V.

With the application of a 0 V bias, the received signal amplitude was 0.125 mV which corresponds to -46.82 dB with respect to the source. As the bias was increased to 12 V, the received amplitude decreased to 0.080 mV corresponding to a 2.92×10^{-3} gain and -50.69 dB with respect to the source. This is a 3.87 dB reduction of the power absorbed with respect to the 0 V applied bias. This power reduction is over 50% total THz absorption by the device with respect to the 0 V applied bias.

It is also important to note that heat can play a part in the absorption of infrared and

THz radiation [27]. However, it can be assumed that this modulation was not because of heat due to the method of testing employed. After the application of 12 V there was a current of 34 mA which will have heated the device. However, it can be argued that heat did not play a part in the modulation because, if that were true, then modulation should have also been observed during the application of the negative bias, which came directly after the 12 V bias.

After the 24 V bias was applied, the device was found to be no longer operational. It is believed that at such a high bias, the 300 nm oxide broke down and created a short within the MOS capacitor like structure across the oxide.

After this bias, reflected power was taken again at 15 V and 0 V. However, the reflected power at both 15 V and 0 V were equivalent indicating that no modulation was occurring. The device was removed from the test set up and was hot to the touch. This made it clear that the device was no longer operational.

Figure 7.10 shows the calculated dBm by the oscilloscope from the received voltage of the total reflected power at given applied electric fields. Equation 7.1 shows the conversion of the received voltage to dBm:

In which V_r is the voltage amplitude and V_0 is 1 mWatt which is the standard reference voltage for the oscilloscope.

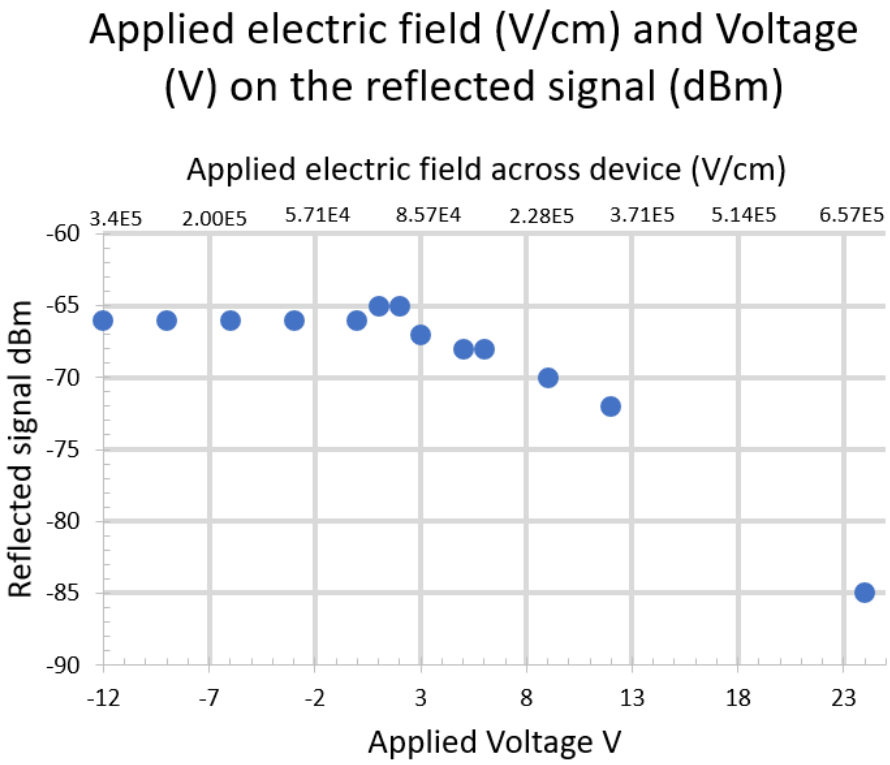

Figure 7.10: A plot taken of the dBm change with the calculated electric field from the applied bias to characterize the level of modulation in the reflected power.

Figure 7.10 shows that the device can modulate the signal by changing the amount it absorbs the THz radiation. Voltages were initially applied gradually to the device to see how that changes the reflected power and how much was being absorbed. At a negative electric field, there was little to no change and the reflected power remained constant. However, as the electric field increased the reflected power in turn decreased significantly. This is indicative of more THz radiation being absorbed from the source by the modulator. Regardless, there is an obvious relationship between the application of a bias across the device stack and the amount of THz radiation the graphene monolayer absorbs.

From Figure 7.10 the modulation that was achieved follows what has been found on graphene plasmonic absorption of THz radiation. As mentioned in Chapter 3 and 4,

experimental [1, 5, 12, 18, 27, 32] and theoretical research groups [4, 13, 24, 29] all observed that materials with a dense 2DEG have a higher absorption of THz radiation. A dense 2DEG allows for an increase in intraband transitions as shown by its Drude-like semi-metal characteristics [41].

The physical operation of this device and the results obtained by the data can be well explained by the charge doping mechanism described in section 2.3. At the Dirac point in the graphene band structure, the density of states is at a minimum [6]. As the charge doping mechanism tunes the Fermi level into the valence or conduction bands, the available intraband states that carriers can move to increases. Therefore, as THz radiation is incident on the device, there is an increase in intraband transition and thus THz absorption [37]. These intraband transitions are characterized by the quantized Landau levels of graphene. Landau levels are quantized energy states resulting from a magnetic field and describe the oscillations of carriers in those states [38]. Landau levels have very high degeneracy allowing for many carriers to be excited to these states. Thus, as the density of states increases with increasing Fermi level, more intraband transitions can occur to these Landau levels.

Very similar results have been obtained by *Sansale et. al.* as mentioned in section 4.2. Their work tested the absorption of a 620 GHz signal on a graphene monolayer that had a back metal gate and a metal ring on top. The graphene monolayer sat on top of a silicon dioxide substrate. They measured a reflected 0.62 THz signal and modulated the absorption with the application of a DC bias. Figure 7.11 shows the summary of their results in normalized reflected power and their theorized position of the graphene's Fermi level.

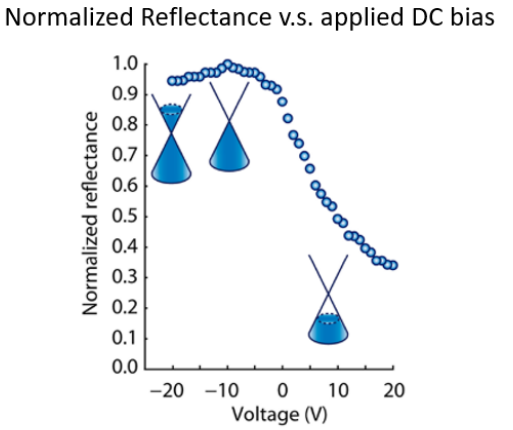

Figure 7.11: Measured normalized reflectance of a 620 GHz signal incident on a graphene monolayer in which varying biases were applied across the stack [37].

As can be seen from their results, the application of a -10 V bias puts the graphene Fermi energy at the Dirac point which leads to a maximum of reflectance and therefore a minimum of absorbance. What was not expected was the minimal absorption at more negative biases that pushed the Fermi energy into the conduction band. However, research done by *Long Ju et. al.* as well as *Sansale et. al.* reports that increased electron concentration increases the light-plasmon absorption and coupling such that as a more negative bias is applied the normalized reflectance will be symmetric about the Dirac point. *Long Ju et. al.* also found that there is significant increase in SPP wave resonance at the 1-4 THz frequencies when excited by far infrared wavelengths which can be further tuned by applied biases ranging from -0.5 to -2.2V [28].

From the work done in references [5, 12, 13, 27, 28, 29] the absorption of the THz radiation can interpreted as the propagation of SPP wave at the THz frequency. However, this was not directly measured from the obtained results. The increase in THz absorption is indicative of an increase in intraband transitions with increasing applied voltages. These

intraband transitions are carriers being excited by the THz radiation to higher energy states. This will lead to a higher intraband conductivity because of its dependance on the Fermi level. Graphene's conductivity is directly related to SPP amplitude because the plasmon amplitude is the magnitude of the AC Drude like conductivity described in chapter 2 [12, 13]. Thus, since characteristics of the SPP wave were not directly measured, the increase of THz absorption could be interpreted as to SPP wave resonance.

8 Conclusions

This work was successful in making a novel graphene based THz modulator. With a modulation of up to 18 dB and absorption of the THz radiation by the graphene monolayer. From the results and operation of the device, there is evidence of charge doping and modulation of the graphene electrical properties. There is also evidence of THz absorption, which has been repeatedly found to be characteristic of SPP waves propagation and graphene plasmonic behavior.

Some process steps proved damaging to the device structure and further research will be needed to better optimize the fabrication of the THz modulator. The two main sources of damage to the structure was the lift off of the thin dielectric layer and wafer saw and cleaning steps.

The cracking and damaging of the thin silicon dioxide layer is a critical issue that will need to be dealt with for further manufacturing of the device. It is believed that this lift off is due to water being trapped in between the graphene monolayer and the thin oxide layer. This pushes up the oxide and forces it to be released. The oxide thermal densification step did limit this damage to areas that were not covered by the Al lines. For future work, different dielectric materials should be considered to achieve better and more pronounced modulation and also limit damage that occurs to the device structure. It has been reported that BN and Alumina are idea dielectrics for graphene based devices [6, 41]. This is because of their similar lattice structures and high dielectric constants.

The next area of the fabricating that must be optimized will be that of the dice separation. Since the Al lines are so thin and cover so much area, it is very easy for particles to scratch

them and remove them from the thin oxide area. Which, as discussed before leads to further thin oxide lift off. Therefore, a different method for dicing the wafer must be employed to limit this particle damage. It would be possible to simply coat the wafer in resist followed by a hard bake then proceed with the wafer saw. The resist could then be ashed away from the chips after a rinse. Another option to avoid the mechanical sawing would be to deep reactive ion etch grooves into the back side of the wafer and then proceed to manually break along the etched grooves.

Further testing of the effect pitch has on THz absorption should also be done on the current devices. It is expected that THz absorption would be increased with decreasing pitch as simulated by *Jornet et. al.* and discussed in Chapter 4. This increase in absorption is due to the increase in THz photon scattering events allowing for an increase in Plasmon coupling [12, 13]. This testing could be further evidence of SPP wave propagation because of the theoretical and simulated models developed by *Jornet et. al.* and *Peres et. al.*.

Future work should also be dedicated to measuring and modulating the resonant THz SPP waves in the graphene based THz modulator. A method would have to be developed to measure the propagating SPP wave. However, it would prove to be a much more practical device as it would allow for a much higher modulation depth because the THz signal can be dynamically tuned [26]. The modulated signal could also be easily directed in a circuit since it will rely on the excitement of the graphene plasmons as opposed to the transmittance of the THz signal.

This work done and results obtained on the graphene based THz modulator shows promising potential for the future high speed THz wireless communications and new processing advances in graphene based devices. These include the transfer of graphene with

RCA based solutions and the patterning of metal on top of graphene based device structure through lift off process steps. It is hoped that these devices will further the initiative of the internet of nano-devices and help bring in a new era of high speed communications surpassing that of current technology.

References

[1] I. Akyildiz and J. Jornet, "The Internet of nano-things," *IEEE Wireless Communications*, vol. 17, no. 6, pp. 58–63, dec 2010. [Online]. Available: http://ieeexplore.ieee.org/document/5675779/

[2] D. M. Slocum, E. J. Slingerland, R. H. Giles, and T. M. Goyette, "Atmospheric absorption of terahertz radiation and water vapor continuum effects," *Journal of Quantitative Spectroscopy and Radiative Transfer*, vol. 127, pp. 49–63, 2013. [Online]. Available: http://dx.doi.org/10.1016/j.jqsrt.2013.04.022

[3] U. Kumar, "Carbon Nanotube Radio," in *Carbon Nanotubes - From Research to Applications*. InTech, jul 2011. [Online]. Available: http://www.intechopen.com/books/carbon-nanotubes-from-research-to-applications/carbon-nanotube-radio

[4] M. Dyakonov and M. Shur, "Shallow water analogy for a ballistic field effect transistor: New mechanism of plasma wave generation by dc current," *Phys. Rev. Lett.*, vol. 71, pp. 2465–2468, Oct 1993. [Online]. Available: https://link.aps.org/doi/10.1103/PhysRevLett.71.2465

[5] Z. Fei, A. S. Rodin, G. O. Andreev, W. Bao, A. S. Mcleod, M. Wagner, L. M. Zhang, Z. Zhao, M. Thiemens, G. Dominguez, and et al., "Gate-tuning of graphene plasmons revealed by infrared nano-imaging," *Nature*, vol. 487, no. 7405, p. 82–85, 2012.

[6] M. Bokdam, P. A. Khomyakov, G. Brocks, and P. J. Kelly, "Field effect doping of graphene in metal|dielectric|graphene heterostructures: A model based upon first-principles calculations," *Phys. Rev. B*, vol. 87, p. 075414, Feb 2013. [Online]. Available: https://link.aps.org/doi/10.1103/PhysRevB.87.075414

[7] J. M. Jornet and I. F. Akyildiz, "Channel modeling and capacity analysis for electromagnetic wireless nanonetworks in the terahertz band," *IEEE Transactions on Wireless Communications*, vol. 10, no. 10, pp. 3211–3221, October 2011.

[8] F. Schwierz, "graphene transistors," *nature nanotechnology*, vol. 5, 2010. [Online]. Available: www.nature.com/naturenanotechnology

[9] P. R. Wallace and P. R. W. Ace, "The Band Theory of Graphite," Tech. Rep., 1947. [Online]. Available: https://journals.aps.org/pr/pdf/10.1103/PhysRev.71.622

[10] T. Cusati, G. Fiori, A. Gahoi, V. Passi, M. C. Lemme, A. Fortunelli, and G. Iannaccone, "Electrical properties of graphene-metal contacts," *Nature Scientific Reports*, vol. 7, 2017.

[11] A. V. Zaretski and D. J. Lipomi, "Processes for non-destructive transfer of graphene: widening the bottleneck for industrial scale production," *Nanoscale*, vol. 7, pp. 9963–9969, 2015. [Online]. Available: http://dx.doi.org/10.1039/C5NR01777G

[12] J. M. Jornet, N. Thawdar, E. Woo, and M. A. Andrello, "Temporal dynamics of frequency-tunable graphene-based plasmonic grating structures for ultra-broadband terahertz communication," *Proc.SPIE*, vol. 10206, pp. 10 206 – 10 206 – 11, 2017. [Online]. Available: https://doi.org/10.1117/12.2262885

[13] N. M. R. Peres, Y. V. Bludov, A. Ferreira, and M. I. Vasilevskiy, "Exact solution for square-wave grating covered with graphene: surface plasmon-polaritons in the terahertz range," *Journal of Physics: Condensed Matter*, vol. 25, no. 12, p. 125303, 2013. [Online]. Available: http://stacks.iop.org/0953-8984/25/i=12/a=125303

[14] Y. Yang, G. Kolesov, L. Kocia, and E. J. Heller, "Graphene Terahertz Absorption," *arXiv e-prints*, p. arXiv:1705.06267, 2017. [Online]. Available: https://arxiv.org/pdf/1705.06267.pdfhttp://arxiv.org/abs/1705.06267

[15] X. Wang and S. A. Tretyakov, "Toward Ultimate Control of Terahertz Wave Absorption in Graphene," 2018. [Online]. Available: https://arxiv.org/pdf/1712.01708.pdf

[16] D. A. D. A. McQuarrie, *Physical chemistry : a molecular approach*. Sausalito, Calif. : University Science Books, [1997] ©1997. [Online]. Available: https://search.library.wisc.edu/catalog/999849410402121

[17] D. J. Gray, A. N. McCaughan, and B. Mookerji, "Crystal structure of graphite , graphene and silicon," 2009.

[18] S. Kim, I. Jo, D. C. Dillen, D. A. Ferrer, B. Fallahazad, Z. Yao, S. K. Banerjee, and E. Tutuc, "Direct measurement of the fermi energy in graphene using a double-layer heterostructure," *Phys. Rev. Lett.*, vol. 108, p. 116404, Mar 2012. [Online]. Available: https://link.aps.org/doi/10.1103/PhysRevLett.108.116404

[19] T. Kleine-Ostmann, P. Dawson, K. Pierz, G. Hein, and M. Koch, "Room-temperature operation of an electrically drivien terahertz modulator," *Appl. Phys. Lett*, vol. 84, p. 3555, 2004. [Online]. Available: https://doi.org/10.1063/1.1723689

[20] L. A. Falkovsky and A. A. Varlamov, "Space-time dispersion of graphene conductivity," *The European Physical Journal B*, vol. 56, no. 4, pp. 281–284, apr 2007. [Online]. Available: http://www.springerlink.com/index/10.1140/epjb/e2007-00142-3

[21] X. Gao, H. Li, X. Huang, C. Gui, and B. Sun, "Statistical physics Gibbs ensemble theory application to Internet system," in *2010 International Conference on E-Health Networking Digital Ecosystems and Technologies (EDT)*. IEEE, apr 2010, pp. 327–330. [Online]. Available: http://ieeexplore.ieee.org/document/5496568/

[22] G. D. Mahan, *Green's Functions at Finite Temperatures*. Boston, MA: Springer US, 1990, pp. 133–238. [Online]. Available: https://doi.org/10.1007/978-1-4613-1469-1_3

[23] S. Xiao, T. Wang, X. Jiang, X. Yan, L. Cheng, B. Wang, and C. Xu, "Strong interaction between graphene layer and fano resonance in terahertz metamaterials," *Journal of Physics D Applied Physics*, vol. 50, p. 195101, 05 2017.

[24] P. A. Khomyakov, G. Giovannetti, P. C. Rusu, G. Brocks, J. Van Den Brink, and P. J. Kelly, "First-principles study of the interaction and charge transfer between graphene and metals." [Online]. Available: https://journals.aps.org/prb/pdf/10.1103/PhysRevB.79.195425

[25] X. Yao, C. Wang, W. Wang, and J. M. Jornet, "On the achievable throughput of energy-harvesting nanonetworks in the terahertz band," *IEEE Sensors Journal*, vol. 18, no. 2, pp. 902–912, Jan 2018.

[26] W. Knap, F. Teppe, N. Dyakonova, D. Coquillat, and J. Łusakowski, "Plasma wave oscillations in nanometer field effect transistors for terahertz detection and emission," *Journal of Physics: Condensed Matter*, vol. 20, no. 38, p. 384205, sep 2008. [Online]. Available: http://stacks.iop.org/0953-8984/20/i=38/a=384205?key=crossref.be4a4ac2d020dd71a027ab5ed3d6f5a0

[27] Z. Fei, G. O. Andreev, W. Bao, L. M. Zhang, A. S. Mcleod, C. Wang, M. K. Stewart, Z. Zhao, G. Dominguez, M. Thiemens, M. M. Fogler, M. J. Tauber, A. H. Castro-Neto, C. N. Lau, F. Keilmann, and D. N. Basov, "Infrared Nanoscopy of Dirac Plasmons at the GrapheneÀSiO 2 Interface," *Nano Lett*, vol. 11, p. 10, 2011. [Online]. Available: https://pubs.acs.org/sharingguidelines

[28] L. Ju, B. Geng, J. Horng, C. Girit, M. Martin, Z. Hao, H. A. Bechtel, X. Liang, A. Zettl, Y. R. Shen, and F. Wang, "Graphene plasmonics for tunable terahertz metamaterials," *Nature Nanotechnology*, 2011. [Online]. Available: http://dx.doi.org/10.1038/nnano.2011.146

[29] Z. Q. Li, E. A. Henriksen, Z. Jiang, Z. Hao, M. C. Martin, P. Kim, H. L. Stormer, and D. N. Basov, "Dirac charge dynamics in graphene by infrared spectroscopy," *Nature Physics*, vol. 4, no. 7, pp. 532–535, 2008. [Online]. Available: www.nature.com/naturephysics

[30] R. A. Lewis, "A review of terahertz sources," p. 374001, 2014. [Online]. Available: https://iopscience.iop.org/article/10.1088/0022-3727/47/37/374001/pdf

[31] Y.-M. Lin, C. Dimitrakopoulos, K. A. Jenkins, D. B. Farmer, H.-Y. Chiu, A. Grill, and P. Avouris, "100-GHz Transistors from Wafer-Scale Epitaxial Graphene," *Science*, vol. 327, no. 5966, pp. 662–662, 2010. [Online]. Available: www.sciencemag.org/cgi/content/full/327/5966/662/DC1http://www.sciencemag.org/cgi/doi/10.1126/science.1184289

[32] P. K. Singh and S. Sonkusale, "High Speed Terahertz Modulator on the Chip Based on Tunable Terahertz Slot Waveguide," *Scientific Reports*, vol. 7, 2017. [Online]. Available: www.nature.com/scientificreports

[33] R. Kersting, G. Strasser, and K. Unterrainer, "Terahertz phase modulator," *Electronics Letters*, vol. 36, no. 13, p. 1156, 2002. [Online]. Available: https://digital-library.theiet.org/content/journals/10.1049/el{_}20000837

[34] Q. Y. Wen, W. Tian, Q. Mao, Z. Chen, W. W. Liu, Q. H. Yang, M. Sanderson, and H. W. Zhang, "Graphene based all-optical spatial terahertz modulator," *Scientific Reports*, vol. 4, 2014. [Online]. Available: www.nature.com/scientificreports

[35] I. Brener, M. J. Cich, H.-T. Chen, D. M. Mittleman, W. L. Chan, and A. J. Taylor, "A spatial light modulator for terahertz beams," *Applied Physics Letters*, vol. 94, no. 21, p. 213511, 2009. [Online]. Available: https://doi.org/10.1063/1.3147221

[36] Y. Zhang, S. Qiao, Z. Yang, S. Liang, Z. Feng, and Q. Chen, "Gbps THz external modulator based on the high electron mobility transistor-metamaterial," in *2015 IEEE MTT-S International Microwave Workshop Series on Advanced Materials and Processes for RF and THz Applications (IMWS-AMP)*. IEEE, jul 2015, pp. 1–3. [Online]. Available: http://ieeexplore.ieee.org/document/7324927/

[37] B. Sensale-Rodriguez, R. Yan, S. Rafique, M. Zhu, W. Li, X. Liang, D. Gundlach, V. Protasenko, M. M. Kelly, D. Jena, L. Liu, and H. G. Xing, "Extraordinary control of terahertz beam reflectance in graphene electro-absorption modulators," *Nano Letters*, vol. 12, no. 9, pp. 4518–4522, sep 2012. [Online]. Available: http://pubs.acs.org/doi/10.1021/nl3016329

[38] F. Wendler and E. Malic, "Doping-dependent intraband carrier dynamics in Landau-quantized graphene," *Physical Review B*, vol. 93, no. 3, p. 35432, 2016. [Online]. Available: https://core.ac.uk/download/pdf/70615810.pdf

[39] R. Han, Z. Hu, C. Wang, J. Holloway, X. Yi, M. Kim, and J. Mawdsley, "Filling the THz Gap," *IEEE Microwave Magazine*, vol. 20, no. 4, pp. 80–93, 2019. [Online]. Available: https://hangroup.mit.edu/wp-content/uploads/2019/03/IEEE{_}Filling{_}the{_}Gap{_}Published.pdf

[40] D. Franz, S. Kaassamani, D. Gauthier, R. Nicolas, M. Kholodtsova, L. Douillard, J.-T. Gomes, L. Lavoute, D. Gaponov, N. Ducros, S. Fevrier, J. Biegert, L. Shi, M. Kovacev, W. Boutu, and H. Merdji, "All semiconductor enhanced high-harmonic generation from a single nano-structure," *Nature Scientific Reports*, vol. 9, no. 5663, 2019. [Online]. Available: https://doi.org/10.1038/s41598-019-41642-yhttp://arxiv.org/abs/1901.02279

[41] V. B. Mohan, K.-t. Lau, D. Hui, and D. Bhattacharyya, "Graphene-based materials and their composites: A review on production, applications and product limitations," *Composites Part B: Engineering*, vol. 142, pp. 200–220, jun 2018. [Online]. Available: https://www.sciencedirect.com/science/article/pii/S1359836817344426

[42] W. Liu, H. Li, C. Xu, Y. Khatami, and K. Banerjee, "Synthesis of high-quality monolayer and bilayer graphene on copper using chemical vapor deposition," *Carbon*, vol. 49, no. 13, pp. 4122–4130, nov 2011. [Online]. Available: https://www.sciencedirect.com/science/article/pii/S0008622311004106

[43] X. Li, W. Cai, J. An, S. Kim, J. Nah, D. Yang, R. Piner, A. Velamakanni, I. Jung, E. Tutuc, S. K. Banerjee, L. Colombo, and R. S. Ruoff, "Large-area

synthesis of high-quality and uniform graphene films on copper foils." *Science (New York, N.Y.)*, vol. 324, no. 5932, pp. 1312–4, jun 2009. [Online]. Available: http://www.ncbi.nlm.nih.gov/pubmed/19423775

[44] X. Liang, B. A. Sperling, I. Calizo, G. Cheng, C. A. Hacker, Q. Zhang, Y. Obeng, K. Yan, H. Peng, Q. Li, X. Zhu, H. Yuan, A. R. Hight Walker, Z. Liu, L.-m. Peng, and C. A. Richter, "Toward Clean and Crackless Transfer of Graphene," *ACS Nano*, vol. 5, no. 11, pp. 9144–9153, 2011. [Online]. Available: https://doi.org/10.1021/nn203377t

[45] A. V. Zaretski, H. Moetazedi, C. Kong, E. J. Sawyer, S. Savagatrup, E. Valle, T. F. O'Connor, A. D. Printz, and D. J. Lipomi, "Metal-assisted exfoliation (mae): green, roll-to-roll compatible method for transferring graphene to flexible substrates," *Nanotechnology*, vol. 26, no. 4, p. 045301, 2015. [Online]. Available: http://stacks.iop.org/0957-4484/26/i=4/a=045301

[46] L. Malard, M. Pimenta, G. Dresselhaus, and M. Dresselhaus, "Raman spectroscopy in graphene," *Physics Reports*, vol. 473, pp. 51–87, 2009. [Online]. Available: www.elsevier.com/locate/physrep

[47] Michrochem Corp, "LOR and PMGI Resists," 2015. [Online]. Available: www.microchem.com

1